Computational Particle Mechanics
https://doi.org/10.1007/s40571-025-01042-8

Application of the PFEM to the study of blood flows and their interactions with highly deformable artery walls, including rupture

Jeanne Delhez[1,2] · **Martin Lacroix**[1] · **Jean-Philippe Ponthot**[1]

Received: 22 May 2025 / Revised: 17 July 2025 / Accepted: 19 July 2025

Abstract

Cardiovascular diseases are the leading cause of mortality worldwide, with projections indicating a concerning rise in related deaths. Computational models offer promising tools to understand the hemodynamics and biomechanical mechanisms underlying vascular failure. In particular, Fluid-Structure Interaction (FSI) algorithms have found significant applications in cardiovascular engineering. This study aims at demonstrating the relevance of the Particle Finite Element Method (PFEM). to model fluid–structure interactions between artery walls and blood flows, and assess the corresponding biomechanical aspects. For this, the flow–structure interaction problem is addressed using a partitioned approach with a strong coupling of the PFEM (for the fluid) and FEM (for the solid) models. Both Newtonian and Casson fluid models, as well as a Mooney–Rivlin hyperelastic model for the deformation of blood vessels, are incorporated. The numerical simulations successfully describe a wide range of situations, from the ejection of blood from the left ventricle to the dynamics of an abdominal aortic aneurysm. To the best of our knowledge, this work describes the very first applications of the PFEM to the study of blood flows in FSI simulations. It is also original by the explicit description of the rupture of the artery wall. Although the model could still be improved, for instance by introducing a turbulence model to deal with high–speed flow through the valve or considering anisotropic hyperelastic models for vessels, the results demonstrate the high potential of this method for describing the interactions of blood flows with the deforming artery walls.

Keywords PFEM · Fluid–structure interaction · Cardiovascular diseases · Aneurysm · Aortic valve · Rupture

1 Introduction

Cardiovascular diseases are a significant threat to human health. In 2021, cardiovascular conditions claimed the lives of 20.5 million people worldwide, representing one–third of all deaths. The upward trend is also alarming, with projections suggesting that by 2030, cardiovascular diseases will cause more than 23 million deaths worldwide per year [1]. Improving our understanding of the hemodynamics and biomechanical mechanisms of vascular failure is crucial to support the development of better diagnostic and therapeutic techniques for cardiovascular diseases [2]. In this context, the use of computational models holds great promises [3]. Numerical models give indeed access to parameters that are difficult to measure directly but are critical for the assessment of the diagnosis and progression of diseases. For instance, the Wall Shear Stress (WSS) is not directly measurable in a blood vessel but is a well–known factor for the initiation and advancement of atherosclerosis, and it is also associated with the risk of arterial complications such as rupture [4]. In addition, when combined with advanced imaging techniques, numerical models can be used to generate detailed three–dimensional representations of patient–specific blood vessels and their function [3, 5]. Such simulations can facilitate pre–operative planning, allowing surgeons to assess the impact of interventions on blood flow patterns and vessel mechanics. The ability to simulate patient–specific geometries and conditions has paved the road for personalized medicine, allowing clinicians to gain insight into disease progression and develop personalized treatments for cardiovascular pathologies [6, 7].

Fluid-Structure Interaction (FSI) algorithms have found significant applications in cardiovascular engineering, in

✉ Jeanne Delhez
j.delhez@uliege.be

[1] Aerospace and Mechanical Engineering, University of Liège, Liège, Belgium

[2] BioMechanics (BMe), Katholieke Universiteit Leuven, Leuven, Belgium

Published online: 09 September 2025

coupling simulations of blood flows with the mechanical responses of blood vessels. Many FSI models have, for example, been developed to investigate the dynamics of abdominal aortic and cerebral aneurysms, providing crucial quantitative and qualitative insights for assessing the various risk factors linked to aneurysms [8–11]. FSI–based heart models have also been created to simulate the complex motions of heart valves as they open and close, capturing the fluid dynamics within the heart chambers. Moving–grid methods (like the Arbitrary Lagrangian-Eulerian (ALE)) are used in the majority of studies and ensure an accurate calculation of blood rheological properties and shear stresses near the blood leaflet interface [12]. However, the need for a frequent remeshing (induced by the large amplitude of the deformation undergone by the very thin leaflets) is a challenging and expensive computational step. For this reason, the Immersed Boundary Method (IBM) which relies on an Eulerian formulation and thus a fixed–grid approach, has often been preferred to the ALE approach. In particular, Bavo et al. [13] concluded that for two–dimensional aortic heart valve geometries, the differences between ALE and IBM are unsubstantial, but that ALE faces major grid quality distortion when it is used in simulating three–dimensional geometry of the aortic valve. Gao et al. [14], for instance, developed a left ventricle two–way FSI model to simulate a complete cardiac cycle using the IBM, while Lemmon and Yoganathan [15] used the IBM approach to develop a three–dimensional FSI model to simulate the leaflets kinematics of bioprosthetic valves. Fixed–grid methods, however, have to interpolate the solution data near the blood leaflet interface, which consequently results in imprecise calculation of important flow parameters, such as WSSs on the leaflets. Meshless methods have been able to counter the problems faced by grid–based FSI methods in terms of accuracy, as well as ease of handling large deformations and complex geometries without remeshing. Mao et al. [16], for instance, applied an implicitly coupled FSI algorithm based on Smoothed Particle Hydrodynamics (SPH) to investigate the leaflets dynamics of a transcatheter aortic valve. So far, however, meshless methods have been only occasionally applied to heart valve simulations, and problems of consistency and stability are reported. Therefore, in this work, we explore the application of the Particle Finite Element Method (PFEM) as an alternative method [17, 18]. In essence, the PFEM is a particle method because all the properties of the flow are attached to the particles. However, the governing equations are integrated on a mesh using the classical Finite Element Method (FEM) in a purely Lagrangian manner. This provides both the flexibility of meshless methods and the robustness of the FEM. While the PFEM has been developed and is generally applied to hydrodynamic engineering or manufacturing [19–21], among others, this study seeks to explore its potential application in the field of biomedical engineering. The particular biomedical applications considered in Sects. 3 to 5 benefit from the general advantages of the PFEM. In particular, the large amplitude movements of the leaflets of the aortic valve during the cardiac cycle and the large deformations of the artery wall in case of aneurysm growth and rupture both involve significant modifications of the computational domain that would, in a Lagrangian framework, demand a frequent remeshing but can be handled in a very efficient and robust way with the PFEM. This advantage stems from the fact that a complete remeshing can be avoided with the PFEM. The PFEM mesh is built on particles that move with the fluid. When remeshing, the nodes of the previous mesh are retained, and it is therefore sufficient to perform a Delaunay triangulation on the cloud of nodes. As the complete solution is entirely determined by the nodal values, i.e., the velocity, pressure, and density of the particles located at the mesh nodes, and since the nodes are preserved during remeshing, the solution does not need to be projected onto the new mesh. Thus, in such a case, there is absolutely no diffusion.

The PFEM has seen very limited applications in biomedical contexts, including the study of blood flows. Del Pin et al. [22], for instance, studied with the PFEM the flow within a simplified centrifugal blood pump under various operating conditions, as well as the steady flow through a patient–averaged model of the inferior vena cava. To the best of the author's knowledge, however, it is the first time that the PFEM is applied to the simulation of blood flows and their interactions with artery walls. As a proof of concept, the following study intends to examine the use of the PFEM in coupled fluid–structure interaction models and to analyze the results from a biomechanical point of view. The remainder of the manuscript is organized as follows: Sect. 2 provides an overview of the fluid–structure interaction strategy adopted in this study and reports the constitutive laws considered. In Sect. 3, a two–dimensional model of the aortic valve is presented. The simulation of an axisymmetric Abdominal Aortic Aneurysm (AAA) is considered in Sect. 4, with results of the explicit simulation of its rupture in Sect. 5. The final section presents a description of future work needed to progress more firmly toward actual biomedical problems.

2 Mathematical and numerical modeling

2.1 Governing equations

2.1.1 Fluid solver

Blood flows are studied by solving the mass and momentum balance equations for an incompressible fluid written as

$$\nabla \cdot \mathbf{v} = 0 \quad \text{in } \Omega_f(t) \times [0, T] \tag{1}$$

$$\rho \frac{D\mathbf{v}}{Dt} = \rho \mathbf{b} - \nabla p + \nabla \cdot \boldsymbol{\tau} \text{ in } \Omega_f(t) \times [0, T] \tag{2}$$

where ρ and $\mathbf{v}$ are the fluid density and its velocity, respectively, p is the pressure, $\boldsymbol{\tau}$ is the viscous stress tensor (deviatoric part of the Cauchy stress tensor), and $\rho\mathbf{b}$ are the body forces. The above equations must be solved in the fluid domain $\Omega_f(t)$, which can change with time t due to the deformation of the vessel walls.

For a generalized Newtonian fluid, the viscous stress tensor is related to the strain rate tensor

$$\mathbf{D} = \frac{1}{2}(\nabla\mathbf{v} + \nabla^{\mathrm{T}}\mathbf{v}) \tag{3}$$

by means of

$$\boldsymbol{\tau} = 2\mu(\mathbf{D})\mathbf{D} \tag{4}$$

where the viscosity μ is allowed to depend on the strain rate. The viscosity is a constant if the fluid is truly Newtonian.

In the PFEM, the continuum is initially discretized using a set of points, referred to as particles, which carry all the mathematical and physical information about the fluid. A PFEM mesh composed of triangles (in 2D) or tetrahedra (in 3D) is built on the set of particles using a standard Delaunay triangulation algorithm [23], with the particular implementation available through the Computational Geometry Algorithm Library (CGAL) [24]. The boundary of the (possibly multiply connected) fluid domain is identified with the α–shape technique [25]. The pruned Delaunay tessellation defines the mesh on which a standard Galerkin approach with linear interpolation functions is applied to solve the differential problem. The resulting instability is handled with a Petrov–Galerkin pressure stabilization technique [26]. The implicit discretization of the Lagrangian semi–discrete equations leads to a system of nonlinear equations that must be solved by an iterative method. A few Picard iterations are usually enough to reach convergence and advance the solution. Alternatively, a Newton–Raphson algorithm can be used.

Although the characteristic size of the finite element mesh can initially be defined to best suit the configuration being studied, the displacement of nodes due to the flow can make the particles concentrate too much in some regions while other regions are described by too few particles. This issue is addressed by adding and removing particles during remeshing. The physical quantities (velocity, pressure, density) attributed to newly created particles are deduced from the current finite element solution [27].

For a detailed description of the PFEM and its implementation, refer to [19].

2.1.2 Solid solver

The accurate modeling of the large deformations of blood vessels and tissues asks for appropriate numerical techniques accounting for the corresponding nonlinear processes. The structural solver used in this work is Metafor, an object–oriented finite element code for the simulation of solids submitted to large deformations using an Updated Lagrangian formalism [28, 29]. At any given time t, Metafor solves a discrete version of the momentum balance equation

$$\rho\frac{D^2\mathbf{x}}{Dt^2} - \nabla\cdot\boldsymbol{\sigma} = \rho\mathbf{b} \qquad \text{in } \Omega_s(t)\times[0,T] \tag{5}$$

where $\Omega_s(t)$ is the volume occupied by the solid in the current configuration, $\mathbf{x}(\mathbf{X},t)$ is the current position of the material particle that was located at $\mathbf{X}$ in the initial configuration, $\rho(\mathbf{x},t)$ is the current density, $\boldsymbol{\sigma}(\mathbf{x},t)$ is the Cauchy stress tensor, and $\rho\mathbf{b}(\mathbf{x},t)$ are the body forces.

Metafor uses a FEM discretization of the principle of virtual work on the deformed configuration. This leads to the semi–discrete equations

$$\mathsf{M}_s\mathbf{a} + \mathbf{f}_{\mathrm{int}} = \mathbf{f}_{\mathrm{ext}} \tag{6}$$

where $\mathbf{a}$ is the nodal accelerations vector, M_s is the mass matrix, and $\mathbf{f}_{\mathrm{int}}$ and $\mathbf{f}_{\mathrm{ext}}$ are the vectors of internal and external forces, respectively. Time integration is performed with the generalized–α method [30, 31]. The system of equations is treated implicitly and solved using a predictor/corrector scheme based on the Newton–Raphson algorithm.

2.1.3 PFEM–FEM coupling

The flow–structure interaction problem is addressed using a partitioned approach with the strong coupling of the PFEM and FEM models described in this section. A subdomain partitioned coupling strategy is used in which the governing equations of the fluid and solid are solved sequentially in the corresponding domains $\Omega_f(t)$ and $\Omega_s(t)$. The two domains are considered separate entities, but share a common interface, $\Gamma(t)$, at which the interaction occurs. Mathematically, the coupling conditions at the fluid–solid interface are defined by the continuity of the displacements and surface tractions at the interface, i.e.,

$$\mathbf{u}_f^{\Gamma} = \mathbf{u}_s^{\Gamma} \tag{7}$$

$$\mathbf{t}_f^{\Gamma} = -\mathbf{t}_s^{\Gamma} \tag{8}$$

where $\mathbf{u}_f^{\Gamma}$ and $\mathbf{u}_s^{\Gamma}$ are the displacement fields at the interface between the fluid and solid domains, respectively, where the surface tractions on the fluid side are given by $\mathbf{t}_f^{\Gamma} = (-p\mathbf{I}+\boldsymbol{\tau})\cdot\mathbf{n}_f$, and where $\mathbf{t}_s^{\Gamma} = \boldsymbol{\sigma}\cdot\mathbf{n}_s$ denotes the corresponding surface tractions on the solid. The normal unit vectors $\mathbf{n}_f$ and $\mathbf{n}_s$ are both pointing outwards from their respective domains.

The FEM and PFEM solvers are coupled by a Dirichlet–Neumann scheme, in which the displacements/velocities at the solid–fluid interface resulting from the solution over

the solid domain are used as Dirichlet boundary conditions for the fluid domain, while the surface tractions on $\Gamma(t)$ computed by solving the fluid problem are prescribed, as Neumann boundary conditions, to the solid. The whole process (described in [32] and [33]) enables to reformulate the coupling conditions (7)-(8) as a fixed–point problem

$$\mathsf{u}_s^\Gamma = \mathcal{T}(\mathsf{u}_s^\Gamma) \tag{9}$$

where $\mathcal{T}$ is a global nonlinear transfer operator.

In practice, since the PFEM and FEM solvers are independent, the fluid and solid problems are solved in a staggered way and iterations are required to solve the nonlinear fixed–point problem (9). A first guess of u_s^Γ is used to compute the fluid solution, which allows the computation of surface tractions to be prescribed to the solid. When injected in the solid problem, these provide a new estimate $\hat{\mathsf{u}}_s^\Gamma$ of the nodal displacements. The procedure is repeated until $\mathsf{u}_s^\Gamma = \hat{\mathsf{u}}_s^\Gamma$. Many different iterative algorithms are available, such as the block Gauss–Seidel method with dynamic under–relaxation [34], the quasi–Newton algorithm with inverse least–square [35], or the multi–vector Jacobian approach [36].

In this iterative process, the displacements and surface tractions are not exchanged as continuous functions of space but only through the nodal values of their finite element discretization. Therefore, unless the fluid and solid meshes are conformal at the fluid–structure interaction interface, the data must be interpolated to transfer the nodal data from one solver to the other. This is done using the Radial Basis Functions (RBF) [33].

In terms of computer implementation, the PFEM–FEM coupling uses a high–level approach in which the fluid and solid solvers are considered as abstract black boxes, see e.g., [32]. The flexibility of the coupling environment is achieved by wrapping the solvers in a Python layer that provides a driving and communicating channel. The wrapping procedure is implemented using the Simplified Wrapper and Interface Generator (SWIG) tool [37]. The fluid and solid solvers operate without exposing their internal algorithms. As a result, the (FSI) coupling algorithm interacts solely with the input and output data of these solvers provided by their respective Python wrappers.

2.2 Constitutive models

2.2.1 Fluid

Plasma itself is a Newtonian fluid, but the presence of other cells induces a non–Newtonian behavior [38]. The reason for this is that, at low shear rates, the erythrocytes have the ability to form a primary aggregate structure of rod–shaped stacks of individual cells called rouleaux [39]. The viscosity of whole blood demonstrates a nonlinear decrease with increasing shear rate. Beyond a certain shear rate threshold, however, the viscosity is nearly constant and blood can be considered to behave as a Newtonian fluid. The shear thinning behavior of whole blood is described using a Casson model [40]. In addition to the shear thinning properties, the Casson model also introduces a minimum shear stress τ_y that must be applied for blood to start flowing [41]. The nonlinear relation between shear stress τ and shear rate $\dot{\gamma}$ ($\dot{\gamma} = \sqrt{2\,\mathbf{D} : \mathbf{D}}$) is described mathematically by

$$\begin{cases} \tau = \mu(\dot{\gamma})\dot{\gamma} & \text{if } |\tau| \geq \tau_y \\ \dot{\gamma} = 0 & \text{if } |\tau| < \tau_y \end{cases} \tag{10}$$

with

$$\mu = \left(\sqrt{\mu_\infty} + \sqrt{\frac{\tau_y}{|\dot{\gamma}|}}\right)^2 \tag{11}$$

with the yield stress τ_y and the asymptotic dynamic viscosity μ_∞.

The discontinuous nature of the Casson model associated with the yield stress makes it challenging to implement in a numerical code. To circumvent this problem, the strategy proposed by Shahzad et al. [42] is implemented. The discontinuous constitutive law is replaced by the continuous approximation

$$\mu(\dot{\gamma}) = \left[\sqrt{\mu_\infty} + \sqrt{\frac{\tau_y}{|\dot{\gamma}|}}\left(1 - \mathrm{e}^{-\sqrt{m|\dot{\gamma}|}}\right)\right]^2 \tag{12}$$

where m is a regularization coefficient. This viscosity is thus used without explicitly considering any yield stress. If the shear rate $\dot{\gamma}$ is large with respect to $1/m$, then (12) is equivalent to the initial formulation (11). For $\dot{\gamma} \to 0$, (12) introduces a bounded finite viscosity

$$\mu_0 = \left(\sqrt{\mu_\infty} + \sqrt{m\tau_y}\right)^2 \tag{13}$$

while the effective viscosity is infinite in the discontinuous formulation (10). However, the two models are expected to produce similar results in practice since the effective viscosity at low strain rate μ_0 can be made arbitrarily large by adjusting the regularization coefficient m. The actual shear rate can therefore be forced to be arbitrarily small, hence mimicking the effect of the yield stress. A value of 200 s for the regularization coefficient m provides an accurate approximation of the theoretical constitutive law in the whole range of shear rate anticipated in the considered flow.

2.2.2 Solid

During its deformation, a body occupies different configurations. The transformation can be described by the mapping

$$\mathbf{x} = \mathbf{x}(\mathbf{X}, t) \tag{14}$$

where $\mathbf{X}$ denotes the reference position of a particle and $\mathbf{x}$ is the current position at time t. The deformation of a material vector $d\mathbf{x}$ is given by

$$d\mathbf{x} = \mathbf{F} d\mathbf{X} \tag{15}$$

where

$$\mathbf{F} = \frac{\partial \mathbf{x}}{\partial \mathbf{X}} \tag{16}$$

is the deformation gradient tensor or Jacobian matrix of the deformation. The determinant of the deformation gradient tensor is called the Jacobian and is denoted by J. It describes the change of volume of an infinitesimal volume of material from the reference $\mathbb{V}_0$ to the current configuration $\mathbb{V}(t)$.

The deformation gradient tensor describes both the rigid rotation of the body and its stretching. The latter can be extracted from $\mathbf{F}$ using the left Cauchy–Green deformation tensor, defined as

$$\mathbf{B} = \mathbf{F}\mathbf{F}^{\mathrm{T}} \tag{17}$$

The quasi-incompressibility of hyperelastic materials can be enforced by introducing the modified version of the deformation gradient tensor $\bar{\mathbf{F}}$ defined by

$$\bar{\mathbf{F}} = J^{-1/3}\mathbf{F} \tag{18}$$

This adjusted deformation gradient is such that

$$\det \bar{\mathbf{F}} = 1 \tag{19}$$

and captures therefore the isochoric part of the deformation. Using this volume preserving part of $\mathbf{F}$, a new left Cauchy—Green tensor can be defined by

$$\bar{\mathbf{B}} = \bar{\mathbf{F}}\bar{\mathbf{F}}^{\mathrm{T}} = J^{-2/3}\mathbf{B} \tag{20}$$

Because of their structural component supported by collagen, blood vessel walls exhibit a soft and flexible structure, and the blood flow through the arteries can significantly modify the vessel radius. Therefore, it is appropriate to use a hyperelastic model for simulating vessel walls [43]. In this work, a Mooney–Rivlin material is adopted [2, 44, 45]. The two–parameter strain energy function of this model can be expressed in terms of the reduced invariants $\bar{I}_1$ and $\bar{I}_2$ of the left Cauchy–Green tensor $\bar{\mathbf{B}}$ as

$$W(\bar{I}_1, \bar{I}_2, J) = C_1(\bar{I}_1 - 3) + C_2(\bar{I}_2 - 3) + \frac{1}{2}K\left[(J-1)^2 + \ln^2 J\right] \tag{21}$$

where J is the determinant of the deformation gradient tensor, C_1 and C_2 are two material constants, and K is a penalty coefficient used to enforce quasi–incompressibility.

Consistency with linear elasticity requires that

$$2(C_1 + C_2) = G = \frac{E}{2(1+\nu)} \tag{22}$$

where E is the Young's modulus, ν is the Poisson's ratio and G is the shear modulus. The penalty coefficient K is taken as the bulk modulus, i.e.,

$$K = \frac{E}{3(1-2\nu)} \tag{23}$$

3 Aortic valve

3.1 Modeling

Fluid–structure interaction is particularly appropriate for modeling the dynamics of heart valves, given the mutual dependence between the movement of the valves and the pressure and flow fields within the heart chambers [3]. In order to illustrate the capability of the PFEM to describe the dynamics of the ejection of blood from the left ventricle, we consider here the simplified two–dimensional plane strain model of the aortic valve shown in Fig. 1. This geometry and the parameters listed in Table 1 are that of Ariane et al. [46] and Sun et al. [2]. The fluid domain comprises the left ventricle, two sinuses, and the initial segment of the aorta. The aortic valve is modeled as two flexible leaflets. The main objective of the model is to reproduce the interaction of the flow with the leaflets and the opening/closing of the valve. With this objective in mind, and considering the much larger rigidity of the peripheral walls, only the leaflets are considered as deformable.

The large rotations of the nearly incompressible isotropic leaflets are accompanied by small strains, so that the assumption of linear elasticity according to Hooke's law is considered [48]. The linear elasticity approach used in this work relies on a hypoelastic formulation, which allows the appropriate consideration of large rotations by resorting to the Jaumann (objective) rate of the Cauchy stress [49].

Blood can be described as a Newtonian fluid when it flows through the aortic valve. The pulsatility of the flow and the large velocity shear largely support this approach. By the same token, however, if one takes into account the fact that the flow is accelerated rapidly by the contraction of the ventricle and pushed through a narrow inter–leaflet space, turbulent effects must be taken into account (Reynolds = 3450). In the absence of a turbulence model, blood viscosity is artificially increased by a factor of 10 in the simulations presented here

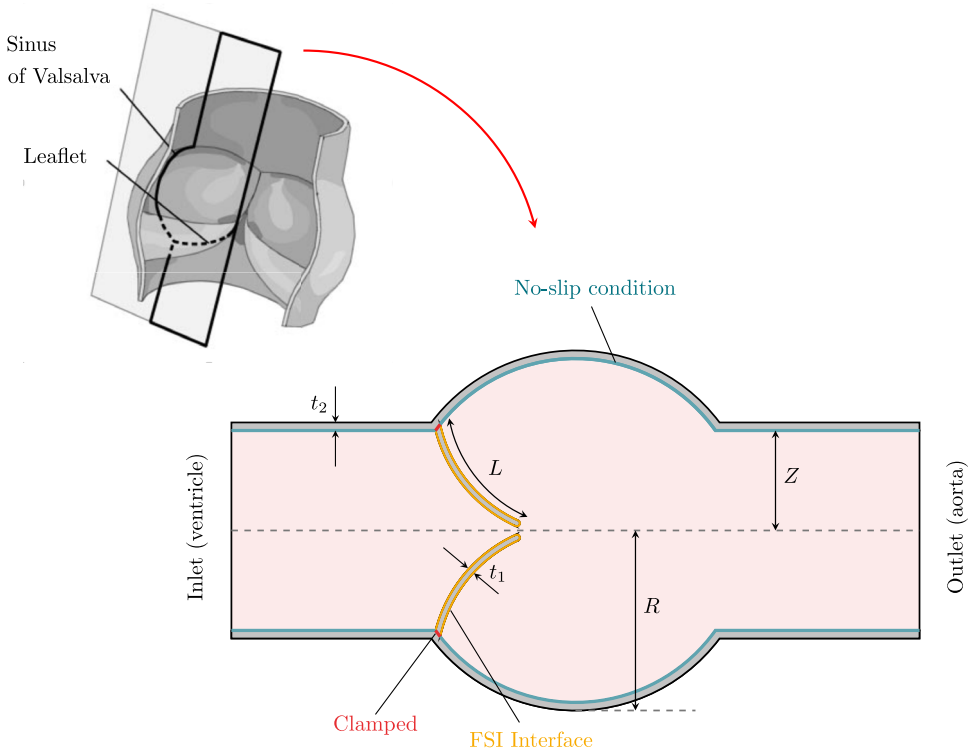

Fig. 1 Geometry of the two–dimensional aortic valve with fluid domain (■), solid domain (■), and boundary conditions (clamped (—), FSI interface (—), and no–slip condition (—)). In essence, a no-slip -condition is also prescribed at the FSI interface. The contact interactions between the two leaflets are handled using a sticking model (implemented in Metafor). Partially reproduced from [47]

Table 1 Geometrical parameters for the aortic valve simulations

Parameters	Values	Units
Aorta radius Z	1.25	cm
Leaflet length L	1.6	cm
Leaflet thickness t_1	0.05	cm
Sinus cavity radius R	2.15	cm
Aortic wall thickness t_2	0.1	cm
Domain total length	6	cm

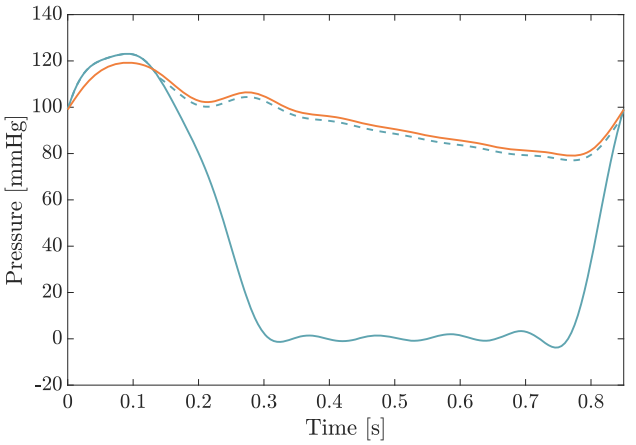

Fig. 2 Time series of the inlet (ventricle) (—) and outlet (aorta) pressures (—) prescribed at the open boundaries of the model domain. To compensate for the impact of the 2D geometry, the ventricular pressure is modified to ensure that the valve resists the applied pressure difference (- -): the maximum pressure difference between the aorta and the ventricle is 2 mmHg

as a proxy for the eddy viscosity to account for the increased momentum diffusion and energy dissipation associated with turbulence. In reality, the turbulence effects vary along the cardiac cycle, but these variations cannot be described without a turbulence model or a Large Eddy Simulation (LES) approach [50].

We chose to drive the model by imposing the temporal pressure variations shown in Fig. 2 on both the ventricular and aortic sides. These boundary data are obtained from Nobari et al. [51]. The inlet and outlet boundary conditions are prescribed via a single layer of Eulerian nodes with assigned pressure values. Since these nodes remain fixed in space, they enable the simulation of fluid inflow and outflow without requiring any physical movement of the inlet and outlet boundaries [52].

The simplification of the geometry associated with the 2D model however comes together with an important modification of the mechanical properties of the aortic valve. In reality, leaflets derive their stiffness from the fact that they are not flat but curved along two axes, and are attached to at least a third of the valve perimeter. These aspects cannot be reproduced in a two–dimensional approach. To overcome this, the artificially reduced resistance to deformation of the leaflets under a given pressure difference is compensated by artificially increasing their Young's modulus. A value of 10^7 Pa,

Table 2 Material parameters for the aortic valve simulations

Parameters	Values	Units
Fluid density ρ^f	1050	kg/m^3
Dynamic viscosity μ	0.038	Pa·s
Leaflets wall density ρ^s	1060	kg/m^3
Leaflets Young's modulus E	10	MPa
Leaflets Poisson's ratio ν	0.45	-

much larger than the actual value of the constitutive material of the leaflets, is therefore used in the simulations, as suggested in [53]. This value has been set by trial and error to match the observed outflow peak velocity. The final choice of material parameters is reported in Table 2. Second, even with such a large value of the Young's modulus, the leaflet would not resist the 100 mmHg pressure difference between the aorta and the left ventricle when the valve is closed. Therefore, the boundary conditions are modified to clip the pressure difference and prevent that the pressure within the sinus cavity exceeds the pressure on the other side of the leaflet by more than 2 mmHg (Fig. 2). This has little influence on the flow, since the two regions are disconnected when this clipping is activated, and on the overall dynamics of the 2D leaflets. The leaflets can deform, open to allow the development of the systolic jet flow, and close when ventricular pressure falls, just like the real aortic valve.

The initial PFEM mesh contains 4960 particles with an increased resolution near the leaflets to capture the larger velocity shear around the leaflets. The leaflets themselves are discretized with a transfinite mesh consisting of 200 elements along each leaflet and 12 elements across. The contact interactions between the two leaflets are handled using a sticking model (implemented in Metafor). This contact model turns out to be necessary to avoid sliding of the two leaflets.

3.2 Results

Snapshots of the flow through the aortic valve are shown in Fig. 3. Initially (1), the valve is closed as the pressure inside the left ventricle is less than that in the aorta. There is no flow through the valve, nor through the aorta. As the heart contracts (2), the valve opens when the pressure difference across the leaflets is large enough to push them toward the sinus cavity. Blood starts then to flow from the left ventricle to the aorta. The opening of the valve and the flow are very dynamic events, which produces a very pulsatile flow. In the Valsalva cavity, the velocity peaks at more than 1 m/s (3). This value is usually reported for a normal healthy patient [54]. As the pulse progresses, vortices appear in the sinus cavity and a backflow develops along the aortic walls (4). The aortic sinus vortex is one of the most important and prevalent fluid dynamic features in the aortic sinuses. It is known to play a crucial role in the context of sinus washout and overall energy efficiency of the aortic valve system [55]. Combined with the decrease of the ventricular pressure, the secondary circulation contributes to the progressive closure of the valve. This, also, is in agreement with the in vivo observations of the flow [56]. With the closing of the valve, the flow from the heart toward the aorta stops while the vortices are progressively damped (5). The velocity progressively goes to zero during diastole before a new cardiac cycle begins (6).

The rapid movement of blood through the constricted valve generates significant shear stresses on the leaflets, and to a lesser extent, around the intersection of the sinus cavity and the aorta. When the valve is fully open, the shear rate $\dot{\gamma}$ reaches 540 s^{-1} on the ventricularis side (i.e., facing the ventricle) of the leaflets (Fig. 4). The maximum appears at the tip of the leaflets. While more quantitative estimates should be confirmed with an even higher resolution modeling to better capture the large gradients in the vicinity of the leaflets, our results are in line with the previous studies and show that the shear rate, and hence the WSS, on the fibrosa side (i.e., facing the aorta) of the leaflets and the sinus section behind them is considerably lower and more dynamic. As reported by Moore et al. [57], these areas are particularly prone to calcification, especially if the vortices in the Valsalva cavity fail to adequately cleanse them.

3.2.1 Impact of calcification

Our model can also be used to study how calcification impacts the normal functioning of the valve. For this, the simulation is repeated by adjusting the thickness t_1 of the leaflets. Instead of the nominal thickness of 0.5 mm, we consider two alternative values of, respectively, 0.75 mm and 0.85 mm. While these changes do not affect the results in any qualitative way, they increase the flexural stiffness of the valves, which are therefore expected to be more resistant to the imposed pressure gradient. Figures 5 and 6 provide a quantitative comparison of the results obtained with the baseline case and the two alternative simulations with thicker leaflets.

The effect of the increased flexural rigidity of the leaflets can first be observed in Fig. 5 of the opening of the valve. This figure suggests that calcification will affect both the duration of the opening and its width. In the nominal configuration, the valves remain open for about 0.28 s. This is about 33% of the cardiac cycle (period $T = 0.85$ s), which is in agreement with experimental data for the normal heart [51]. With the thicker leaflets, the time during which the valve is open decreases to 0.22 s or even 0.20 s for the 0.85–mm–thick leaflets. At the same time, the width of the opening is also strongly reduced by calcification. With the thickest leaflets, the maximum opening is reduced by a factor 2, going from about 13 mm in the nominal run to 6.5 mm for the 0.85–

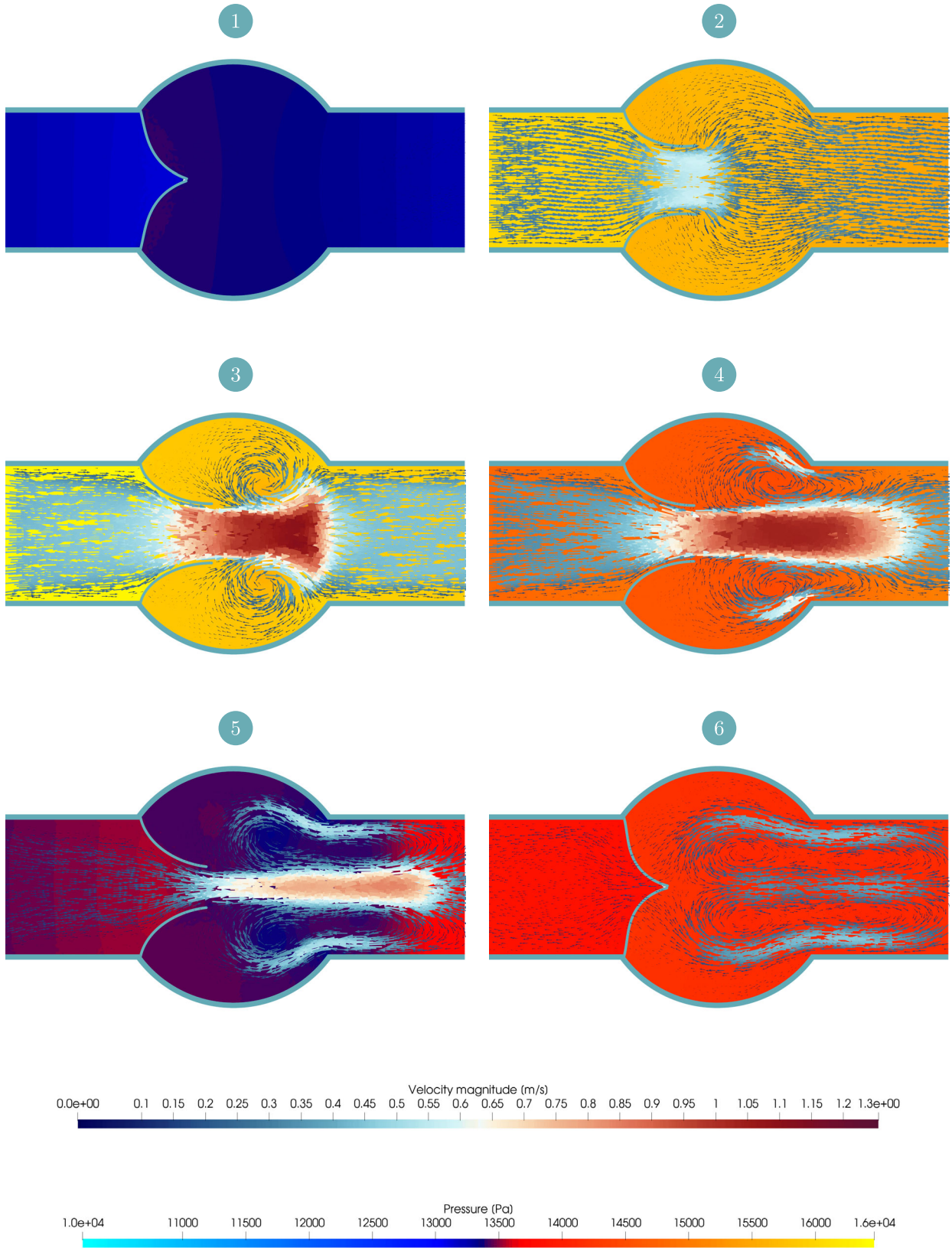

Fig. 3 Pressure (background color) and velocity fields (arrows) at 6 successive moments of the cardiac cycle: (1) $t = 0.00$ s, (2) $t = 0.05$ s, (3) $t = 0.10$ s, (4) $t = 0.15$ s, (5) $t = 0.20$ s, and (6) $t = 0.30$ s

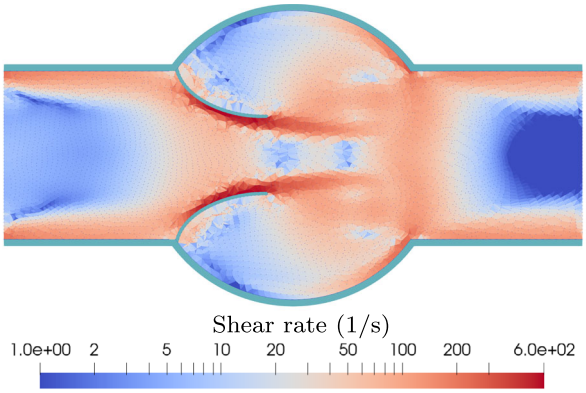

Fig. 4 Shear rate at the time of maximum opening of the aortic valve

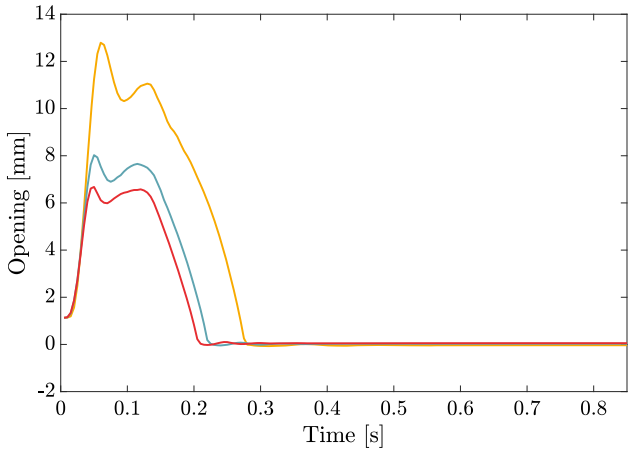

Fig. 5 Evolution of the opening of the valve with time for the nominal configuration with $t_1 = 0.5$ mm (—) and for two alternative configurations with thicker leaflets ($t_1 = 0.75$ mm (—) and $t_1 = 0.85$ mm (—))

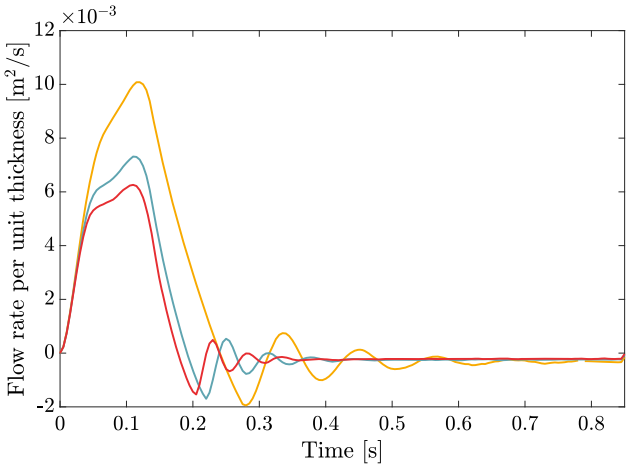

Fig. 6 Evolution of the flow rate (per unit length of transverse direction) with time for the nominal configuration with $t_1 = 0.5$ mm (—) and for two alternative configurations with thicker leaflets ($t_1 = 0.75$ mm (—) and $t_1 = 0.85$ mm (—))

Table 3 Stroke volume per unit length across transverse dimension

Thickness t_1 [mm]	0.5	0.7	0.85
Stroke volume [mm^2]	1377.1	871.4	724.9

mm–thick leaflets. The opening of the valve influences of course the flow rate into the sinuses of Valsalva (Fig. 6). The decreased opening of the thicker leaflets goes with a reduction of the flow rate through the valve. The maximum flow rate decreases and the flow occurs during a reduced period of time. It should be noted, however, that the maximum flow rate is not reduced in proportion to the reduction in valve opening. While the thickest leaflets show a maximum opening that is about half of the opening in the nominal configuration, the corresponding maximum flow rate nevertheless reaches 60% of that of the more flexible leaflets. The reduction in both the maximum flow rate and the duration of the ejection phase for the stiffer leaflets results in a large decrease in stroke volume, the volume of blood ejected with each heartbeat (Table 3). Direct comparison of the raw numbers with physiological values is difficult (as the 2D model only provides an estimate of the flow rate per unit length across the transverse dimension), but the results illustrate how calcification can have a serious impact on the heart ability to pump blood throughout the body.

Clinical studies reveal that calcification of the aortic valve affects the hemodynamics inside the aortic root such as the transvalvular pressure gradient and the WSS on both sides of the leaflets. Prior research has shown that variations in wall shear stress levels on the front and back surfaces of leaflets play a role in calcification formation [58]. As calcification levels rise, WSS levels increase on the front ventricularis surface, but decrease on the back fibrosa surface. Therefore, the WSS gradient between the two surfaces intensifies, potentially triggering mechanobiological mechanisms that further promote calcification, thus perpetuating stenosis over time [59, 60]. Our results are consistent with these findings. The general distribution of the shear rate for calcified leaflets is similar to Fig. 4 but the shear rate at peak systole on the ventricularis surface increases from 540 s^{-1} for the 0.5–mm–thick leaflets, to 580 s^{-1} and 620 s^{-1} in the two calcified cases.

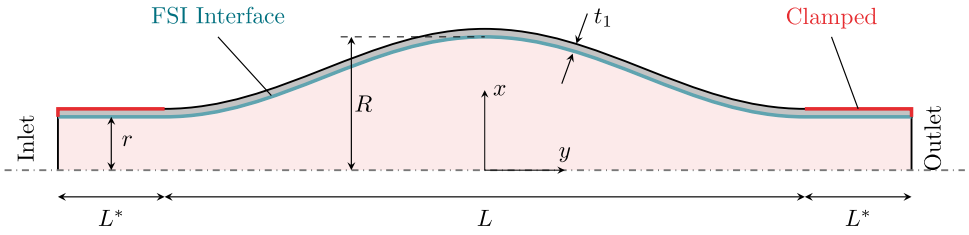

Fig. 7 Geometry of the axisymmetric abdominal aortic aneurysm with fluid domain (■), solid domain (■), and boundary conditions (clamped (—) and FSI interface (—))

Table 4 Geometrical parameters for the abdominal aortic aneurysm simulations. The actual domain is extended upstream and downstream by 2 cm to avoid numerical artifacts and instabilities at the boundaries of the fluid domain

Parameters	Values	Units
Length L	12	cm
Length extension L^*	2	cm
Vessel radius r	1	cm
Aneurysm radius R	2 - 2.5 - 2.75	cm
Thickness t_1	0.15	cm

4 Aneurysm

4.1 Modeling

In this section, we consider the interaction of blood flow with a compliant axisymmetric abdominal aneurysm wall. The aneurysm is assumed to be fully developed with an axisymmetric shape. The geometry is directly inspired from Scotti et al. [9] (Fig. 7). The fluid domain is characterized by a circular cross section with a non–dilated diameter r and a maximum radius R at the midsection of the AAA sac. More precisely, the radius $\phi(y)$ is assumed to vary with the longitudinal coordinate y according to

$$\phi(y) = \begin{cases} r + \dfrac{(R-r)}{2}\left[\cos\left(\dfrac{\pi y}{6r}\right) + 1\right] & \text{if } -6r \le y \le 6r \\ r & \text{if } |y| > 6r \end{cases} \tag{24}$$

The total length of the aneurysm is $L = 12$ cm, which is about the actual length of the abdominal aorta, but the model is extended upstream and downstream with $L^* = 2$ cm segments to avoid spurious oscillations between the inlet/outlet boundary conditions and the moving walls. The geometrical parameters considered in the different simulations are listed in Table 4.

The model is forced by prescribing velocity and pressure time series at the upstream and downstream boundaries of the fluid domain, typical of the time evolution over the cardiac cycle of the parameters in the infrarenal segment of the human abdominal aorta [61] (Figs. 8 and 9). These waveforms describe a pulse repeating every 1 s (period $T = 1$ s). These boundary data define the average velocity value v_a across the inlet section. The actual velocity profile is prescribed as:

$$v = 1.5 v_a (1 - \xi^4) \tag{25}$$

where $\xi \in [0, 1]$ is the relative coordinate measured from the symmetry axis. This profile is relatively flat but ensures that the velocity vanishes at the artery wall.

The time–averaged velocity prescribed at the inlet is about 6 cm/s. The mean Reynolds number is therefore 332 and, as observed by other authors, the flow can be assumed to be laminar in the abdominal aorta [9, 62]. Also, blood is assumed to behave as a Newtonian fluid. The Womersley number (the ratio of the unsteady inertia to viscous effects, here $W = \sqrt{\rho^f R^2/\mu T} = 13.8$ with the geometrical and material parameters of Tables 4 and 5) and the anticipated shear rate are large enough to ignore any yield stress and shear thinning behavior of blood. The aortic segment is fixed at its two extremities, which accounts for the complete tethering of the aorta by the surrounding tissues and organs.

The fluid domain is discretized with 4509 PFEM particles, with a resolution doubled near the fluid–structure interface. The segment of the artery wall in contact with the flow is represented by a transfinite mesh composed of 300×12 linear quadrangular elements. The axisymmetric geometry is modeled by solving the governing equations in the r–z plane, assuming rotational symmetry about the central axis.

We consider first a $R = 2.5$ cm aneurysm with a constant wall thickness of 1.5 mm. The fluid is Newtonian and the artery wall is described with a Mooney–Rivlin model. The material parameters are listed in Table 5.

4.2 Results

The velocity field at three different moments of the cardiac cycle is depicted in Fig. 10. As blood pulses in the artery (1), the peak velocity reaches 42 cm/s in the inlet and outlet segments that are not affected by the aneurysm. By continuity, the velocity is much smaller in the aneurysm itself because of the increased cross section. The flow gently follows the contours of the artery and is essentially unidirectional. When the flow decreases, some weak vortices do, however, appear occasionally both at the entrance and exit cross sections of the

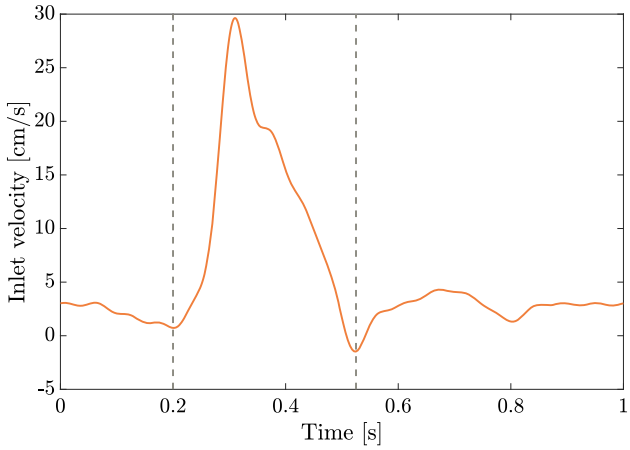

Fig. 8 Inlet velocity waveform reproduced from [61]. The waveform is divided between its systolic (between dotted lines) and diastolic parts

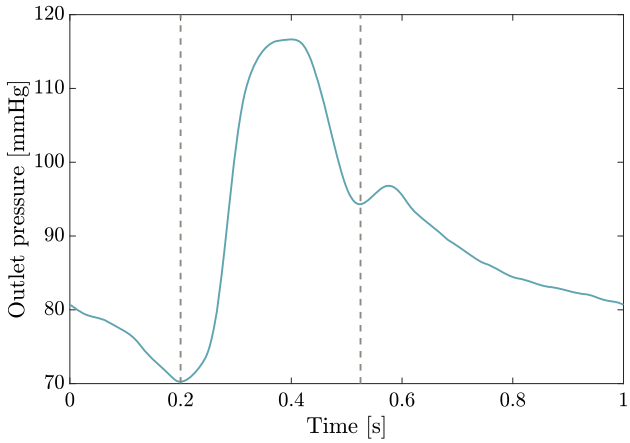

Fig. 9 Outlet pressure waveform reproduced from [61]. The waveform is divided between its systolic (between dotted lines) and diastolic parts

Table 5 Material parameters for the abdominal aortic aneurysm simulations

Parameters	Values	Units
Fluid density ρ^f	1050	kg/m^3
Dynamic viscosity μ	0.0038	Pa·s
Arterial wall density ρ^s	1200	kg/m^3
Arterial wall Young's modulus E	2.7	MPa
Arterial wall Poisson's ratio ν	0.45	-
Mooney–Rivlin parameter C_1	0.584	MPa
Mooney–Rivlin parameter C_2	−0.1185	MPa

aneurysm, where the wall curvature is greatest ((2) and (3)). A small counter–flow corresponding to the dicrotic notch is also observed at time $t' = t - T = 0.5$ s. Wall stresses follow the evolution of pressure with time. The maximum values are therefore observed at the peak systolic pressure. The main effect of the internal pressure is to produce circumferential stresses and a smaller contribution to the longitudinal stresses. The maximum hoop stress reaches 2.49 10^5 Pa, while the maximum von Mises equivalent stress is 2.23 10^5 Pa. The distribution (Fig. 11) is symmetric around midsection with the maximum occurring around the inflection points of the wall, approximately one aneurysm radius away from the middle section. This pattern and the characteristic values closely align with the results of Scotti et al. [9] who study the same configuration (same geometry with aneurysm radius $R = 2.5$ cm, same inlet and outlet waveforms) and report a maximum equivalent von Mises stress of 2.38 10^5 Pa. During the cardiac cycle, the maximum displacement of the wall reaches 1.5 mm in the radial direction around the center of the aneurysm with little variation around this spot, which is also consistent with Scotti et al. [9] although their distribution shows the maximum displacement shortly off–centered.

4.2.1 Influence of the initial size of the aneurysm

To go further with the analysis, we consider two other aneurysms with initial radii of 2 cm and 2.75 cm. All the other parameters are unchanged (thickness of the wall, boundary conditions, material parameters). Results are shown in Fig. 12. Table 6 shows the maximum hoop stress, maximum equivalent von Mises stress, and the range of displacement at mid–aneurysm for the three sizes of the aneurysm. As expected, all the parameters increase with the size of the aneurysm.

The increase in hoop stress and equivalent von Mises stresses with the radius of the aneurysm reflects the usual balance of forces in a cylindrical thin–walled vessel under pressure, i.e.,

$$\sigma_{\text{hoop}} = \frac{Rp}{t_1} \tag{26}$$

(where R is the radius of the vessel and t_1 is the wall thickness). The aneurysm with the larger radius must resist a larger resultant force and is therefore the seat of large stresses. However, the stress grows slightly faster than the size of the aneurysm. This is most likely related to nonlinear geometrical effects, including wall curvature in the radial plane, and the influence of fluid flow. This increase is potentially dangerous because it could induce greater deformation of the arterial wall, with even greater stresses. However, the maximum deformation in the middle section is seen to increase less than proportionally with the radius of the aneurysm,

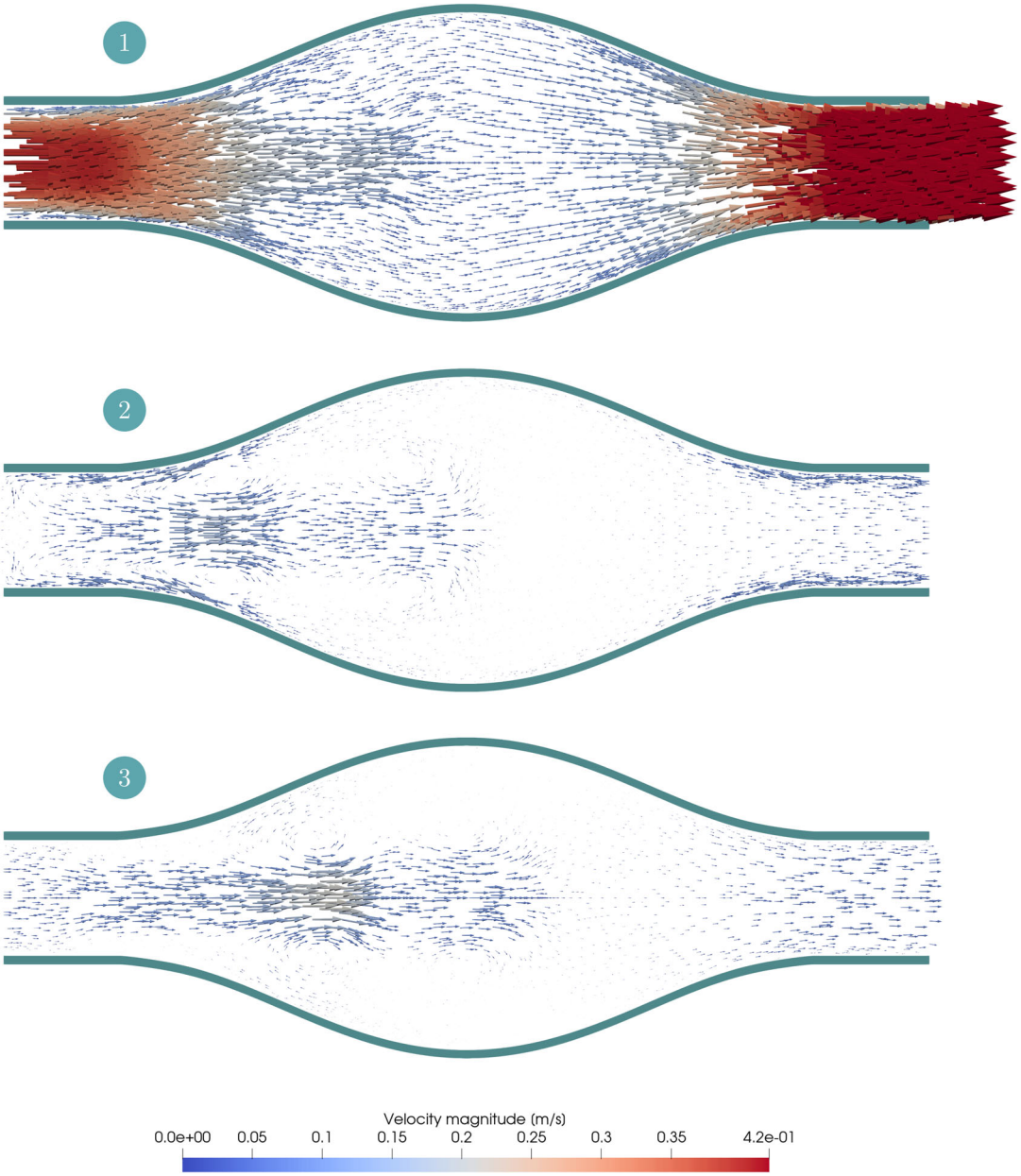

Fig. 10 Velocity field in the 2.5–cm aneurysm at the peak systolic flow ((1) $t' = t - T = 0.32$ s) and two subsequent moments during diastole ((2) $t' = 0.50$ s and (3) $t' = 0.70$ s)

which ensures that the aneurysm remains stable, at least with the stiffness considered in the current simulations.

4.2.2 Three–layer model

The wall of arteries are essentially three–layer structures with each layer (intima, media and adventitia) playing a distinct role in preserving vascular homeostasis and regulating the vascular response to stress or injury [63] (Fig. 13). Many studies simplified the aorta as a single–layer structure, with a uniform thickness and uniform material properties

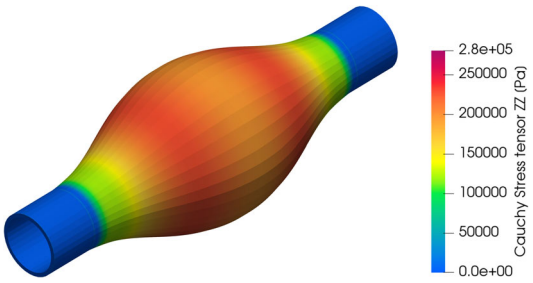

Fig. 11 Circumferential (hoop) stress at systolic pressure of the 2.5–cm aneurysm

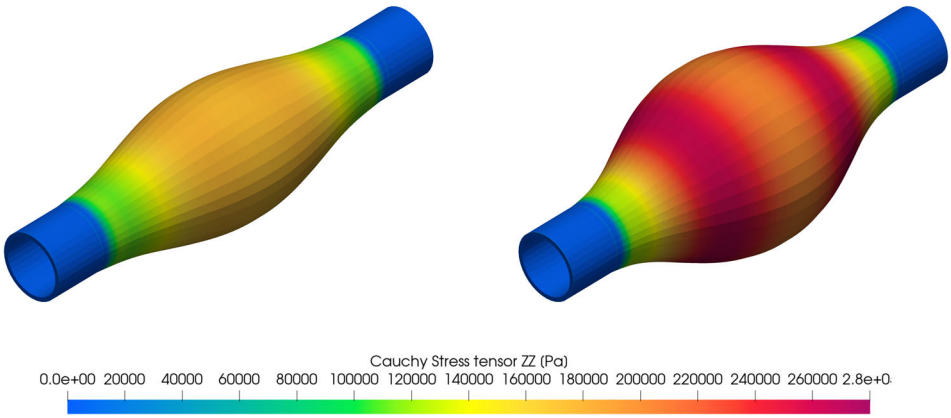

Fig. 12 Circumferential (hoop) stress at systolic pressure of the 2–cm aneurysm (left) and the 2.75–cm aneurysm (right)

Table 6 Sensitivity of key parameters to the size of the aneurysm: maximum hoop stress (σ_{zz}), maximum equivalent von Mises stress (σ_{VM}), and displacement in the middle section of the aneurysm (Δr) (minimum displacement at diastolic pressure and maximum displacement at systolic pressure)

Initial radius R [cm]	σ_{zz} [10^5Pa]	σ_{VM} [10^5Pa]	Δr [mm]	
			min	max
2	2.02	1.799	0.72	1.12
2.5	2.49	2.230	0.89	1.50
2.75	2.77	2.496	1.02	1.66

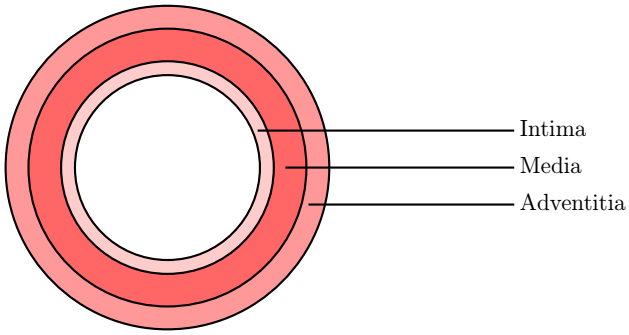

Fig. 13 Schematic view of the three layers of blood vessel wall

throughout the vessel. The three layers, however, have different mechanical properties and contribute thus differently to the vessel stiffness. We therefore introduce a more realistic three–layer structure, for which the mechanical behaviors of the intima, media, and adventitia are described by the Mooney–Rivlin model, and following Simsek et al. [45], the Young's moduli of the three layers are assumed to be in the ratio 1/3/2. These values are derived from bending experiments by Xie et al. [64]. The relative thickness and model constants for the three layers are reported in Table 7. The three layers deform together as a single solid and exhibit similar strains (ignoring the impact of geometrical nonlinearities), i.e., they work in parallel and the equivalent Young's modulus of the three–layer structure is the average of the individual moduli weighted by their relative thickness. The parameters listed in Table 7 ensure that the three–layer wall exhibits the same stiffness as the single–layer model considered initially. The Poisson's ratio is kept at a value of $\nu = 0.45$.

The most interesting aspect of the refined model is related to the stress distribution. The results reveal much larger hoop stresses and equivalent von Mises stresses, about 25% larger, than in the model using only one layer. A quick examination of a cross section through the middle of the arterial wall shows that the maximum hoop stress occurs in the thick and stiff media layer, which provides the greatest contribution to counteracting pressure forces (Fig. 14). The intima,

Table 7 Relative thickness, equivalent Young's modulus, and Mooney–Rivlin parameters for the three layers of the aneurysm wall. The Poisson's ratio is kept at a value of $\nu = 0.45$

Layer	Relative thickness	E MPa	C_1 MPa	C_2 MPa
Intima	0.20	1.174	0.254	−0.052
Media	0.47	3.522	0.762	−0.155
Adventitia	0.33	2.238	0.484	−0.098

on the other hand, does not contribute significantly to the resistance of the wall. Its primary function is known to be the modulation of interactions between the blood and the artery wall, making its role more biological than mechanical [65]. Because of their different composition, the three layers exhibit different mechanical properties. In particular, the risk of rupture in each of these layers should be examined with respect to the ratio of the actual stress to the intrinsic ultimate stress of that layer.

4.2.3 Wall shear stress analysis

The dynamics of aneurysm actually proceeds at two different timescales. So far, we have considered the movements of the artery along the cardiac cycle. The initiation and progression of aneurysms proceed, however, with a longer timescale char-

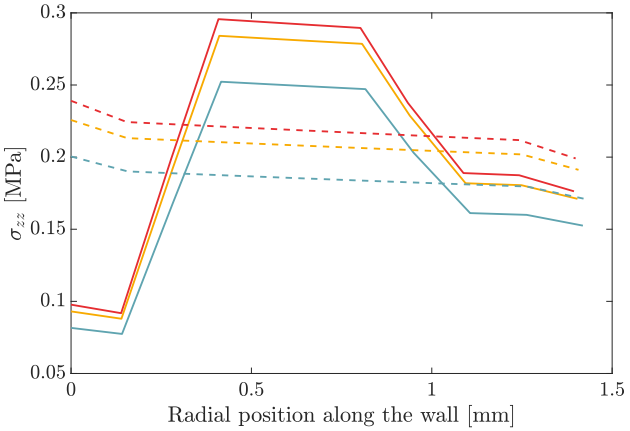

Fig. 14 Cauchy hoop stress (nodal values) variation along the wall for the 2–cm (—), 2.5–cm (—), and 2.75–cm (—) aneurysms. Data are taken in the radial direction, at the mid of the aneurysm sac, at the time of maximum hoop stress. Results correspond to the three–layer model (—) and single–layer model (- -)

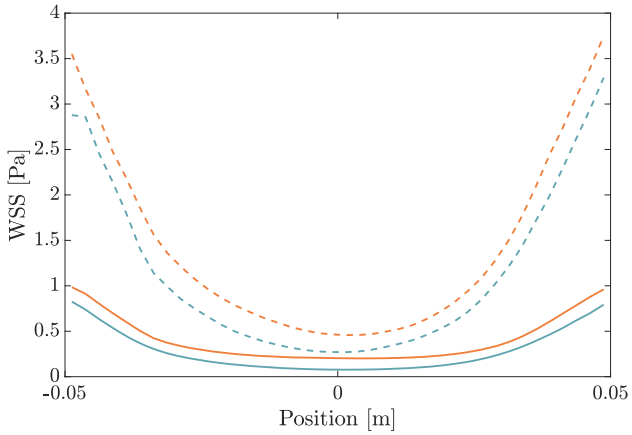

Fig. 15 Time–averaged wall shear stress (—) and maximum wall shear stress (- -) along the artery segment (position y in Fig. 7) using a Newtonian model (—) and a Casson (—) fluid model (τ_y = 0.0035 Pa and μ_∞ = 0.0038 Pa·s). Results correspond to the 2.75–cm three–layer aneurysm

acterizing the biological transformations of the vessel wall. Aneurysms initiation can be caused by an initial weakness in the blood vessel wall, which may be present from birth in some cases, a high blood pressure also resulting in damage and weakening of blood vessels, atherosclerosis, or other diseases resulting in the weakening of the blood vessel wall [66]. The proper description of the corresponding mechanisms requires specific models of the evolution of the damage of the wall over periods of months and years. There is a natural interplay between the models at the short and long timescales. Models of the cardiac cycle can describe the mechanical stress to which the cells of the artery walls are exposed, including the WSS and the cycle of loading/unloading. These parameters are influenced by the geometry of the aneurysm and the stiffness of the artery wall. The latter are determined by the biological response occurring at the longer timescale.

In this work, we do not consider the longer timescales but touch upon some aspects of this two–timescale analysis. Figure 15 shows the Time–Averaged Wall Shear Stress (T–WSS) (obtained by integrating the WSS magnitude over the cardiac cycle) and the maximum WSS computed in the three–layer model of the 2.75–cm aneurysm. The results indicate a reduction of these parameters by a factor of three in the aneurysm with respect to the initial and terminal sections. The small values of the wall shear stress (T–WSS $<$ 0.4 Pa) experienced by the endothelial cells in the sac of large–scale aneurysms are known to create an environment that is favorable to the deposition of plaque and atherosclerosis [67]. This kind of result can be used as an input to a longer timescale model describing the evolution of atherosclerosis on the artery wall. The information on WSS provided by numerical models is valuable because WSS cannot be measured in vivo. Most estimates rely indeed on Poiseuille's law to calculate WSS from blood velocity measured by echo Doppler ultrasound. This is, of course, a crude approximation because it ignores local dynamic and geometrical effects and assumes a constant and fully developed flow.

From a methodological point of view, the results also suggest that the constitutive equation is used to describe the blood rheology matters. While the hoop stress and deformation of the aneurysm are insensitive to the choice between a Newtonian or a Casson fluid model, the time–averaged and maximum WSS values computed with the Casson fluid assumption are, respectively, 22% and 13% higher than the corresponding results computed with a Newtonian model. Given the clinical significance of WSS in atherosclerosis diagnosis, the use of the more realistic Casson fluid model is therefore recommended when assessing the stress acting on endothelial cells.

4.2.4 Aneurysm initiation and stability

The heterogeneity of the wall, especially its thickness, is known to be a significant factor in the risk of AAA rupture. Accurately assessing thickness in patient–specific CT images is challenging due to calcification, thrombus, and indistinct image definition between the inner and outer wall surfaces. However, experimental sampling of wall specimens has revealed that the wall is indeed non–uniform, thinning in response to pulsatility and the progressive expansion of the aneurysm sac [9, 68]. We consider here local thinning as a potential cause of aneurysm initiation.

In the first two models, the wall thickness is assumed to decrease from the nominal value of 1.5 mm at the two extremities of the aortic segment to a local minimum of 1 mm in its center section. The flow is then modeled as previously with

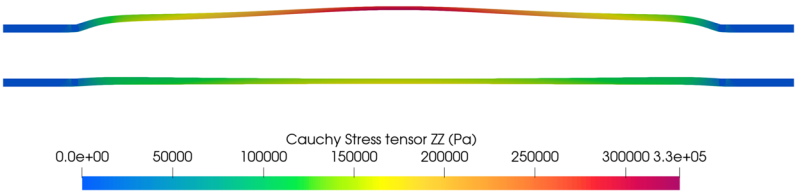

Fig. 16 Deformation and hoop stress in a straight artery segment with a local decreased thickness of 1 mm in the central section at the peak systolic pressure. The upper figure is computed with a Young's modulus of 0.675 MPa, while the lower one shows the behavior of the stiffer wall ($E = 2.7$ MPa)

either a 0.675 MPa Young's modulus, characteristic of the unperturbed artery wall, or with a higher value of 2.7 MPa that is generally measured in aneurysm walls.

The results shown in Fig. 16 illustrate the impact of the stiffness of the artery wall on the initiation of the aneurysm. If the local thinning of the artery is not compensated by an increase of its Young's modulus, the artery wall experiences significant deformations. A maximum radial displacement of 4.20 mm is computed here. If, however, biological remodeling occurs and the Young's modulus increases thanks to the replacement of elastin by collagen, such large deformations can be avoided. Here, a maximum of only 0.52 mm is obtained with the stiffer wall. The deformation not only decreases on account of this physiological adaptation but also the maximum hoop stress. In Fig. 16, this stress component peaks at 0.17 MPa for the adapted artery while the hoop stress reaches 0.33 MPa in the more flexible aorta. These results clearly demonstrate the relevance of the adaptation of the stiffness of the artery to mitigate the influence of a local thinning.

Reducing the wall thickness to 0.75 mm in the central section leads to even more disastrous outcomes (Fig. 17). A stiffer artery, with a modulus of elasticity $E = 2.7$ MPa, can withstand systolic blood pressure without pathological deformation or stress. However, a more flexible artery ($E = 0.675$ MPa) forms a significant bulge, experiencing both extensive deformation and stress. Owing to the Poisson effect, the wall thickness reduces even more, increasing the hoop stress and ultimately causing the aneurysm to rupture.

5 Rupture of aneurysms

5.1 Risk assessment

A comprehensive understanding of the different factors contributing to the propagation of the aneurysm is crucial for the appropriate clinical handling. The surgical criteria for elective AAA repair must carefully consider the risk of rupture against the risk of the repair procedure. Surgery presents indeed an in–hospital mortality rate of about 3–5 % for open repair and 1–2 % for endovascular repair [69].

The size of the aneurysm is a universally recognized factor to forecast rupture. For AAAs, the European Society for Vascular Surgery recommends surgery at a maximum aortic diameter of 55 mm for men and 50 mm for females and patients with increased probability of rupture [70, 71]. Although easy to use in practice, statistics suggest that the size of the aneurysm is probably not the sole useful criterion for risk of rupture: 13% of AAAs with a diameter smaller than 50 mm rupture while 60% of AAAs with a diameter greater than 50 mm remain stable during the patient's lifetime [71, 72]. In addition to the diameter, the expansion rate of an aneurysm is a significant factor in assessing the risk of rupture. An expansion rate exceeding 10 mm per year is considered critical for an AAA. However, the expansion rate might not always be available for clinical assessment due to the requirement for historical patient data [70, 71]. Ideally, the decision to repair an aneurysm should not be guided by maximum transversal dimension and expansion rate alone, but rather by a more reliable criterion associated with the actual rupture potential of the patient–specific artery. Although not directly measurable in vivo, stresses on the aneurysmal wall are believed to be a better rupture risk index and offers better data for surgical evaluation than size and growth rate [73, 74]. As illustrated in the previous section, the highest stress can indeed greatly vary despite identical maximum diameter and similar blood pressure. The wall of an aneurysm is a living and metabolizing structure, able to add and reinforce itself. Enlargement does not necessarily imply increasing the risk of rupture [45].

The use of peak wall stress (i.e., peak principal stress) as a potential predictor of AAA rupture has been explored in several studies [73, 75, 76]. Raghavan et al. [77], for example, found that the peak wall stress for AAAs which either ruptured or were symptomatic was significantly greater than the peak wall stress in electively repaired or asymptomatic AAAs. It is therefore a superior measure than maximum diameter for predicting patients with an unfavorable outcome. The authors also report that the location of peak wall stress is not the point of maximum diameter, but in the posterolateral part of the AAA, which coincides with the area of rupture in patients. The actual risk of rupture depends, however, actually on the ratio of wall stress to the estimated local

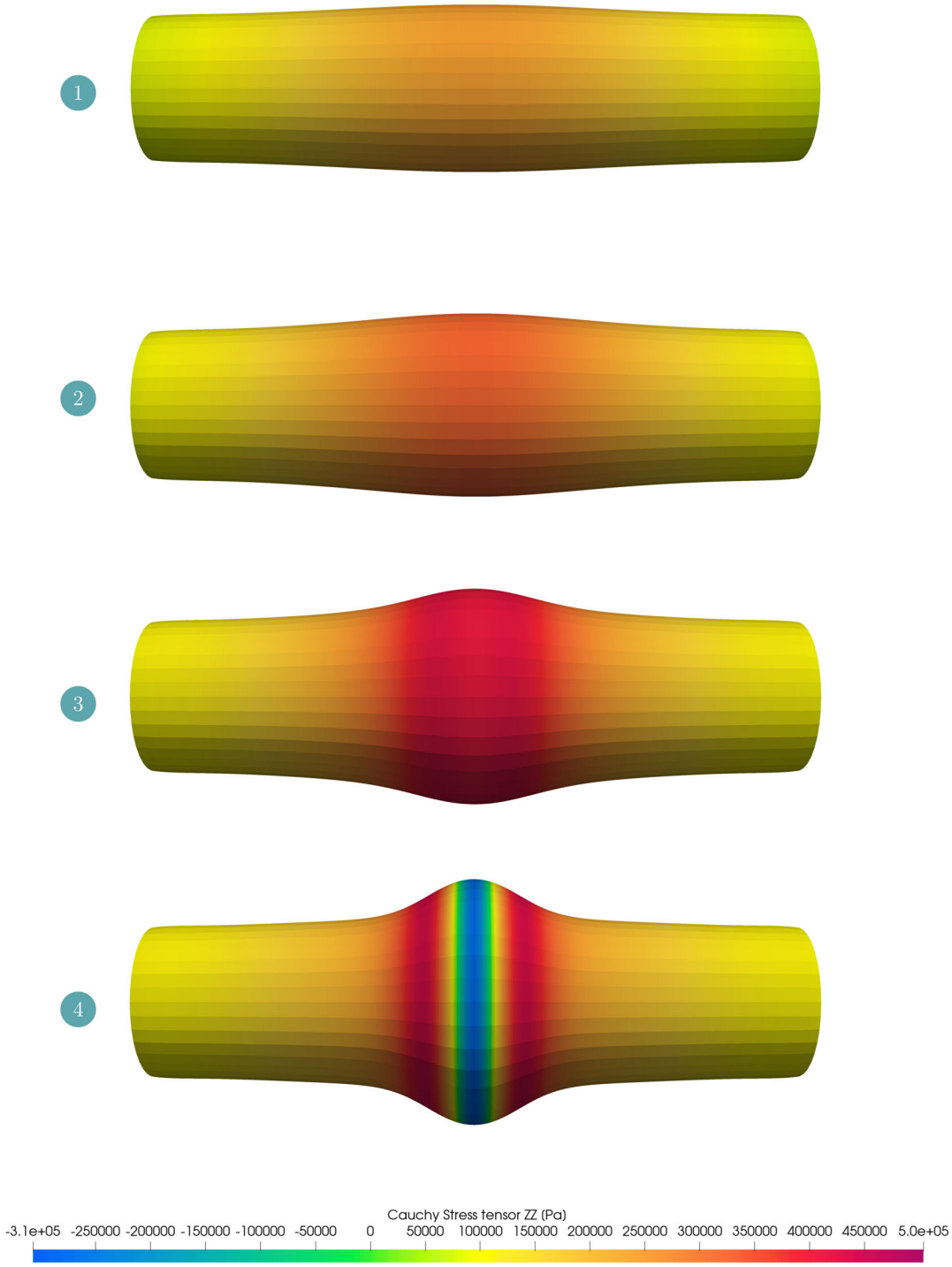

Fig. 17 Deformation and hoop stress in a straight artery segment with a local decreased thickness of 0.75 mm in the central section at four successive moments of the cardiac cycle: (1) $t = 0.395$ s, (2) $t = 0.445$ s, (3) $t = 0.465$ s, and (4) $t = 0.475$ s

wall strength, which defines the Peak Wall Rupture Index (PWRI) [78]. Wall strength does not only vary from patient to patient but also significantly within the same aneurysm. Therefore, wall strength must be carefully evaluated on a patient–specific basis to accurately predict the rupture potential of individual aneurysms [74, 79, 80].

5.2 Numerical modeling and results

In line with the above discussion, rupture of the artery wall is assumed here to occur when the greatest principal component of the stress tensor in a given element exceeds a given threshold, on average over the different Gauss points of the considered element. In Metafor, when the rupture criterion is reached, the corresponding element is simply deleted from the discretization and the deformation and stress fields are updated accordingly [81]. The feasibility of this methodology is demonstrated for two different geometries.

5.2.1 Cerebral berry aneurysm

As a first demonstration of the capability of the code to model the rupture of a blood vessel, we consider the 2D plane strain model of the cerebral aneurysm schematized in Fig. 18. The geometry describes a semi–circular aneurysm on the side of a cerebral vessel and is adapted from Sun et al. [2]. The real dimensions used by Sun et al. [2] are reported in Table 8.

Such a 2D model is greatly simplified as it fails to capture the real balance of forces present in 3D configurations. Specifically, it does not account for the dominant component of the stress tensor, the hoop stress, and how it varies with the local radius of a blood vessel. Consequently, this model should be regarded as a tool model to demonstrate the modeling of rupture. We therefore feel free to introduce more simplifications that make the model further depart from the real problem.

While it was advocated above that the rupture criterion should be based on the largest principal stress, the equivalent von Mises stress is considered here in this preliminary study. In practice, rupture of an element is assumed to occur when the average equivalent von Mises stress over the Gauss points of one given element exceeds 0.2 MPa.

No–slip boundary conditions are applied on the straight outer boundary of the vessel and on the FSI interface (Fig. 18). The fluid model is forced by prescribing the inlet velocity and the outlet pressure. Starting from rest, the flow is allowed to develop for 0.2 s until a velocity of 45 cm/s is reached in the main segment of the vessel. A linear increase of pressure is then prescribed via the outlet boundary condition. A peak of 100 mmHg is reached at time $t = 0.5$ s.

A hypoelastic linear model of the walls of the vessels is used with $E = 5$ MPa and $\nu = 0.45$. Since the simplified 2D geometry does not allow for hoop stresses to balance the internal pressure, the non–dilated part of the vessel wall is fixed on its outer boundary. While the whole upper wall is considered in the solid model, only the aneurysm region is therefore allowed to deform under the internal pressure and flow. Because of the 2D approach, the model also lacks the right features to predict where rupture will occur. We therefore rely on the work of Crompton et al. [82], who analyzed the location of rupture in 289 cerebral aneurysms. In this work, the observed aneurysms are divided lengthwise from the origin to the top of the artery into approximately three equal thirds. The proximal third adjacent to the parent artery is called the neck, the middle third is the body, and the distal third is the apex. Rupture has been observed to occur predominantly through the apex of cerebral aneurysms. To ensure that the model describes the rupture of the aneurysm at a physiologically meaningful location and not in the regions where the fixed boundary conditions are applied to the solid, the wall thickness is increased along the straight part of the vessel and at the base of the aneurysm. In contrast, a local weakening of the aneurysm wall is simulated by introducing a 25% decrease in wall thickness where rupture is reported in clinical observations.

Table 8 Geometrical parameters for the cerebral berry aneurysm simulations

Parameters	Values	Units
Length L	28.8	mm
Width Z	3.6	mm
Height H	1.6	mm
Wall thickness t_1	0.55	mm
Aneurysm thickness t_2	0.3	mm
Aneurysm radius R	3.6	mm

The initial PFEM mesh contains 4392 particles, while the vessel wall is discretized with a transfinite mesh consisting of 690 elements.

Figure 19 shows the results of the simulation. Figure 20 shows the initial flow in the blood vessel with a well developed flow in the straight part and a vortex flushing the aneurysm region. The reduced thickness around the apex can be seen to induce a local maximum of the equivalent von Mises stress (1) (Fig. 19). When blood pressure increases, the rupture threshold is first reached in the corresponding element, which is therefore deleted (2) (Fig. 19). Blood is then accelerated through the hole in the vessel by the very large pressure gradient existing between the inner and outer regions. Blood is ejected at a very high velocity that quickly exceeds 5 m/s. At the same time, the stresses in the artery wall decrease sharply as the pressure inside the aneurysm drops (3) (Fig. 19).

The steep pressure gradient between the ends of the vessel and the aneurysm causes a significant increase in flow

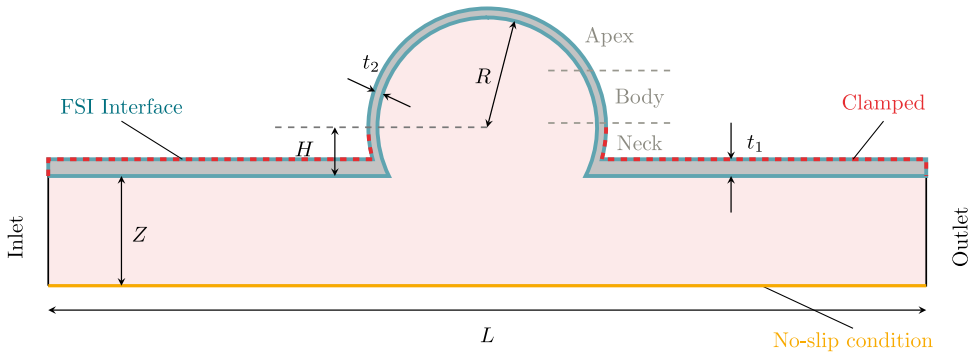

Fig. 18 Simplified cerebral berry aneurysm geometry with fluid domain (■), solid domain (■), and boundary conditions (clamped (- -), FSI interface (—), and no–slip condition (—))

velocity in the straight portion of the vessel. The boundary condition on the velocity imposed at the entrance of the cerebral artery limits the flow rate, so the blood rushes away from the downstream boundary toward the aneurysm and the hole in it.

The rupture of the aneurysm separates the two parts of the wall, which loses its stiffness and deforms significantly as the two parts move apart at approximately 3 m/s (see velocity field in Fig. 21). This rapid movement creates significant stresses at the base of the aneurysm, resulting in a new, somewhat artificial rupture at this point in the last subfigure (4) (Fig. 19).

5.2.2 Axisymmetric abdominal aortic aneurysm

As a second proof of concept of the rupture modeling, we return here to the modeling of the axisymmetric abdominal aneurysm described in Sect. 4 (Fig. 7). Although real aneurysms often have a more complex, truly 3D geometry, the axisymmetric model provides a fair description of many of the features of real aneurysms [83]. However, axisymmetric rupture is much less realistic because it implies that the two parts of the vessel are completely separated when rupture occurs. In general, rupture occurs around some weak point in the arterial wall. Despite its inherent limitations, the axisymmetric model has the ability to represent the balance of forces by accounting for the dominant hoop stress in the artery wall and the dependency of this stress component on the radius of the deformed vessel. A 2–cm aneurysm with a uniform wall thickness and a Mooney–Rivlin model ($C_1 = 0.584$ MPa, $C_2 = -0.1185$ MPa, corresponding to $E = 2.7$ MPa) of the artery material is considered.

The Cauchy stress tensor in an axisymmetric model comprises only the components σ_{xx}, σ_{yy}, σ_{xy}, and σ_{zz}, with the hoop stress σ_{zz} taking much larger values than the other components and acting out of plane with respect to the three other components. As a result, it is the largest principal stress to be used in the rupture criterion. In this section, we consider that rupture occurs when the hoop stress reaches a value of 0.18 MPa on average over the integration points of an element. Note that this value does not have a true clinical meaning but is used here for demonstration purposes. In practice, the accurate modeling of rupture would require the knowledge of the wall strength, which as reported in the introduction to aneurysm rupture, must be evaluated on a patient–specific basis. This critical value is somewhat arbitrarily chosen for the sole purpose of highlighting the fracture phenomenon, but is nevertheless of the same order of magnitude as the peak stress threshold of 0.28 MPa reported by Vorp et al. [80].

Rupture of the axisymmetric aneurysm is illustrated in a dedicated simulation where the flow is allowed to develop in the blood vessel during the initialization phase and pressure is increased gradually until rupture occurs. The model is forced by imposing the evolution of pressure at both the inlet and the outlet. A pressure signal gradually increasing to a value of 100 mmHg is prescribed, but with a phase shift of 0.004 s between the inlet and outlet sections. This describes the propagation of a progressive wave along the artery.

The deformation, rupture, and outward bleeding of the aneurysm simulated under this forcing are shown in Fig. 22. The second subfigure reveals that rupture does not occur where the diameter of the aneurysm is maximum, but around an inflection point of the aneurysm (2). This clearly reflects the stress distribution already observed in Fig. 11. This provides an interesting validation of the model since the results are in agreement with the experimental study carried out by Doyle et al. [84]. By analyzing the location of the rupture of abdominal aortic aneurysms, they also observe that rupture occurs around an inflection point of the aneurysm sac and not in the middle section. This can also be observed in Fig. 22. The occurrence of rupture on the distal part, rather than the proximal part, indicates that while the stress distribution around the middle section is roughly symmetrical, it is not perfectly so, displaying a slight asymmetry due to the dynamics of blood flow within the artery.

The significant pressure difference across the artery wall causes blood to be ejected at approximately 3 m/s through the ruptured element (3). Concurrently, pressure within the artery near the leak decreases, and this pressure gradient relative to

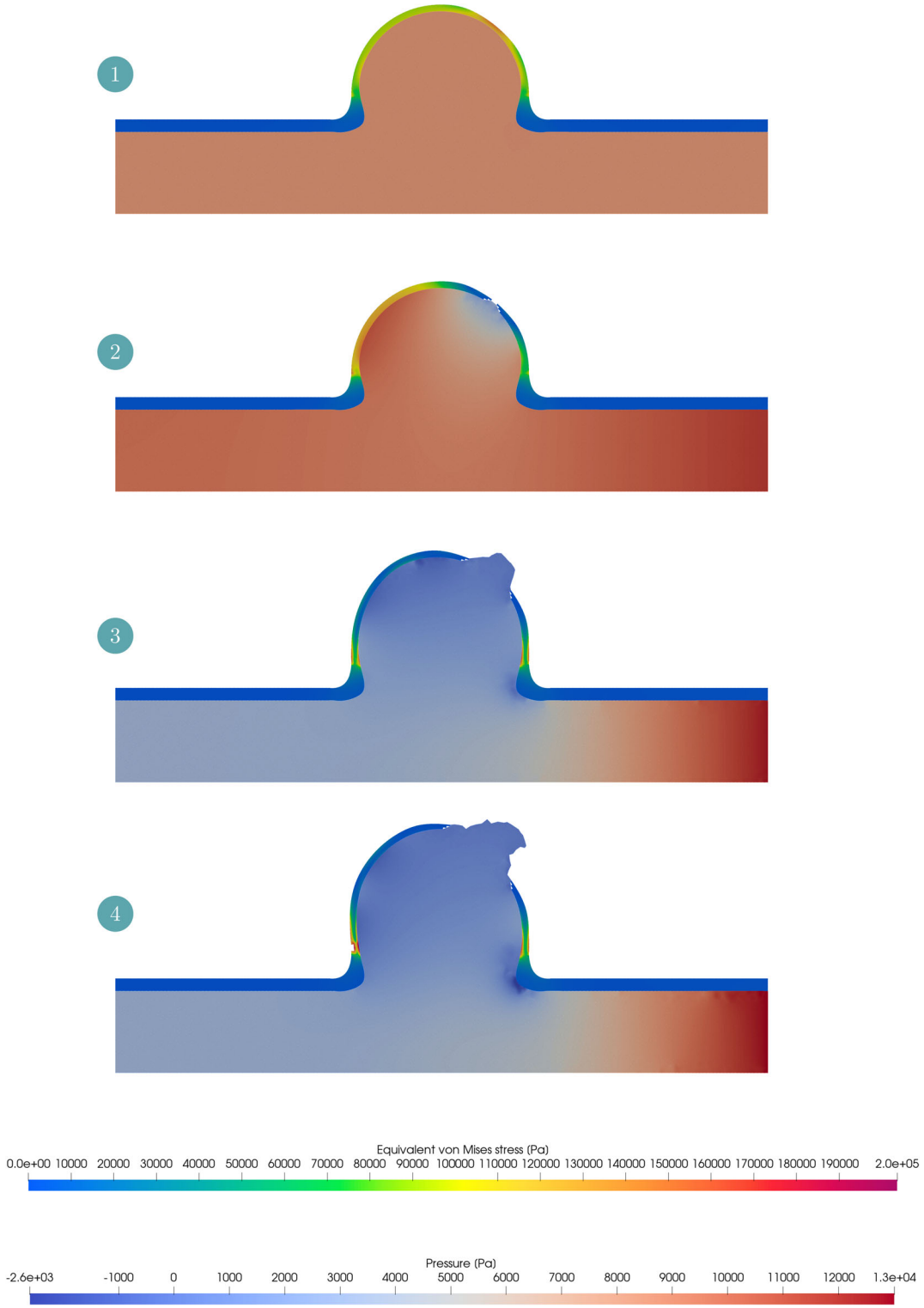

Fig. 19 Deformation and rupture of a cerebral berry aneurysm at four successive times: (1) $t = 0.4780$ s, (2) $t = 0.4785$ s, (2) $t = 0.4910$ s, and (4) $t = 0.4955$ s. Pressure field is related to the fluid, while von Mises stress is related to the solid part. Blood flows from left to right. Rupture occurs in the apex region of the aneurysm

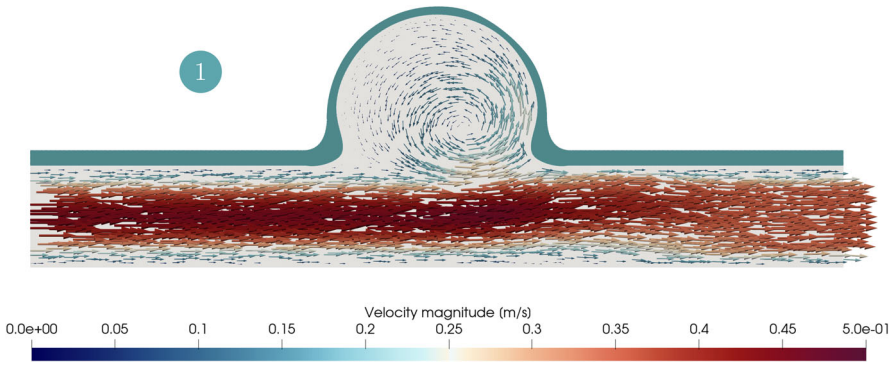

Fig. 20 Velocity field in a cerebral berry aneurysm at time $t = 0.4780$ s (subfigure (1) of Fig. 19)

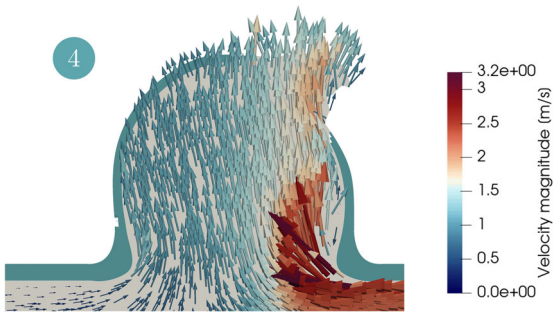

Fig. 21 Velocity field in a cerebral berry aneurysm at time $t = 0.4955$ s (zoom on the hole of subfigure (4) of Fig. 19)

the inlet region causes a swift increase in blood flow within the artery. Approximately 3 ms post–rupture, the velocity at the inlet region doubles, surpassing 1 m/s, resulting in a rapid influx of blood from the upstream region into the aneurysm. With the drop of blood pressure, the forces on the artery wall also decrease sharply, which can be observed on the hoop stress distribution. The later increase of the hoop stress observed in subfigure 4 while blood continues to be ejected through the hole is a numerical artifact (4). The sudden rupture of the artery wall creates a negative pressure wave that propagates through the model domain. Because the inlet pressure is prescribed by the boundary condition, the expansion wave bounces on this boundary and is reflected as a compression wave that affects the whole domain by artificially increasing pressure in the artery.

6 Conclusion and perspectives

The aim of this work was to demonstrate the possibilities offered by the Particle Finite Element Method and the modeling of fluid–structure interactions in the context of the study of the cardiovascular system. To the author's knowledge, it is the first time that the PFEM is applied to problems of this kind. The various models developed in this study highlight the potential of the PFEM to enhance our understanding of hemodynamics and biomechanical processes. This offers significant promises to diagnose cardiovascular diseases and develop new therapeutic methods that could improve patient care. However, there are still numerous limitations that constrain the pertinence of the results and the practical application of these numerical tools in a clinical setting.

As illustrated by the simulation of the opening of the aortic valve, some physiological flows are turbulent and therefore require a proper modeling of the corresponding phenomena. Simple zero–equation models are unsuitable due to the extensive separated regions and significant curvature effects present in turbulent blood flow modeling. Although it will require more computational time, incorporating a two–equation $k - \epsilon$ model would enhance the model versatility. Alternatively, considering that blood flows are only weakly turbulent, a shift toward LES might be considered. This approach would demand higher spatial and temporal resolutions, along with the adoption of Smagorinsky–type modeling for sub–grid scales [85].

Considering their large numerical cost, 3D simulations have not been carried out in this work. While no specific difficulties are anticipated, except the computational load, three–dimensional models of the aortic valve, of arteries and aneurysms would of course allow to increase the fidelity of the simulations with the real physiology and open the way for the practical use of numerical simulations by the clinicians. Three–dimensional models would include the real geometry of blood vessels, with their tortuosity, curvature, details of branching, and local variations of the material properties of their wall that have been found to impact physiologically relevant parameters like the WSS. In the future, simple 3D models and, even more preferably, actual patient–specific geometries reconstructed from imaging data should be considered.

Such next–generation models should also take into account the anisotropic behavior of the biological tissues of the cardiovascular system. In order to account for the realistic material properties of the aortic wall, aneurysmal tissue, and aortic leaflet tissue, the use of a nonlinear, anisotropic, viscoelastic material property should be investigated to take into

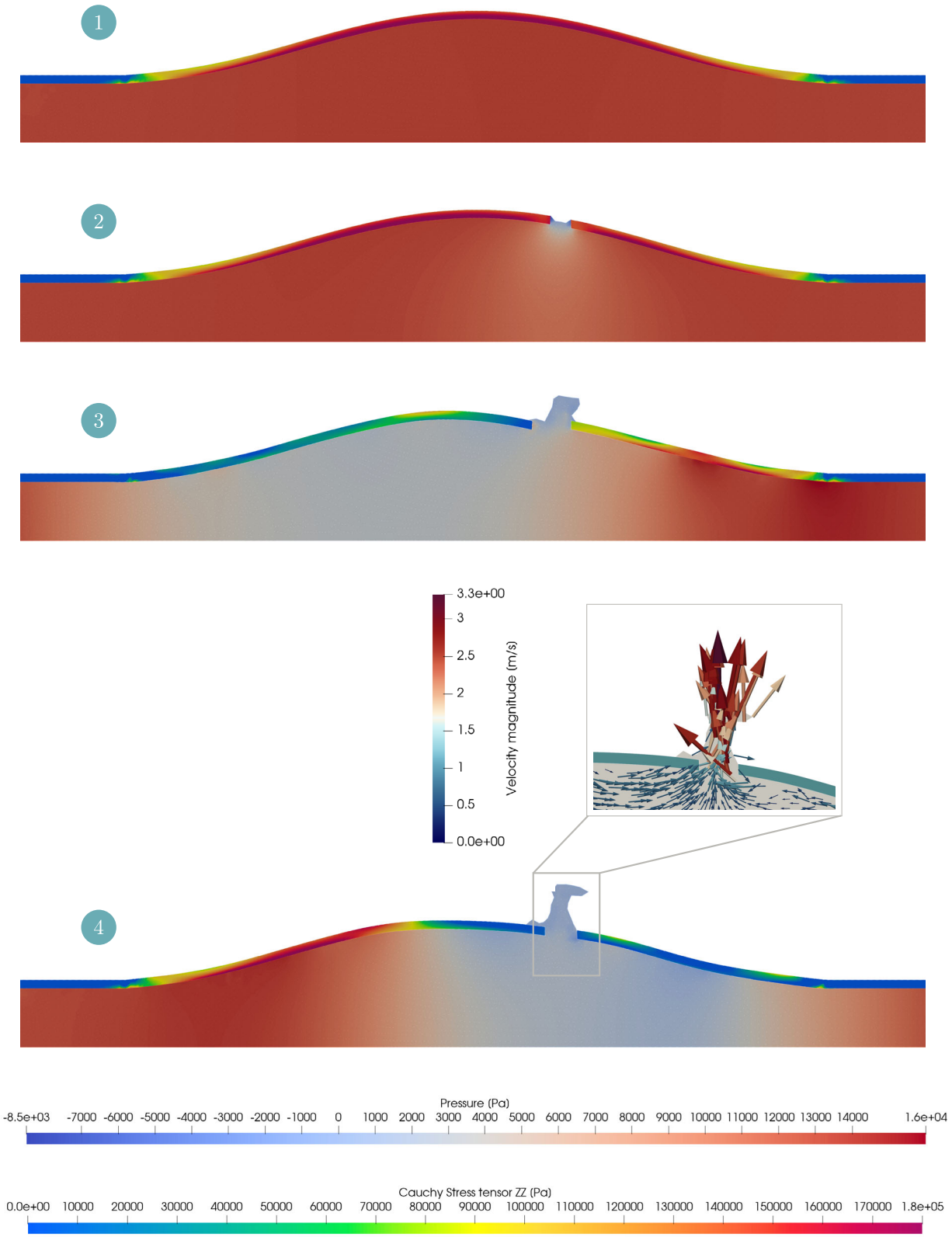

Fig. 22 Deformation and rupture of an axisymmetric abdominal aneurysm at four successive times: (1) $t = 0.1085$ s, (2) $t = 0.1090$ s, (3) $t = 0.1120$ s, and (4) $t = 0.1135$ s (with zoom on the hole with velocity field). Pressure field is related to the fluid while Cauchy stress is related to the solid part. Blood flows from left to right

account the non–collagenous matrix with embedded collagen fibers.

Most importantly however, the model should be extensively validated against experimental data before being applied to tackle real patients issues. Such data are for instance particularly necessary to validate the constitutive laws of biological tissues and the corresponding rupture criteria. When numerical aspects of the codes are validated and robust models are available, an interdisciplinary approach with engineers and physicians must therefore be set up to address the relevance of the results and make further progress.

Acknowledgements This work was supported by the Belgian National Fund for Scientific Research (F.R.S.-FNRS) under the research project PFEM-FSI (PDR reference T.0183.21). Rue d'Egmont 5, 1000 Brussels, Belgium.

Data Availability The data that support the findings of this study are available from the corresponding author, Jeanne Delhez, upon reasonable request.

Declarations

Conflict of interest The authors declare that they have no Conflict of interest.

References

1. World Heart Federation (2023) World Heart Report 2023: confronting the world's number one killer. https://www.who.int/data/data-collection-tools/who-mortality-database
2. Sun WK, Yin BB, Zhang LW, Liew KM (2023) Blood pressure-driven rupture of blood vessels. J Mech Phys Solids 174:105274. https://doi.org/10.1016/j.jmps.2023.105274
3. Hirschhorn M, Tchantchaleishvili V, Stevens R, Rossano J, Throckmorton A (2020) Fluid-structure interaction modeling in cardiovascular medicine—a systematic review 2017–2019. Med Eng Phys 78:1–13. https://doi.org/10.1016/j.medengphy.2020.01.008
4. Laudato M, Mosca R, Mihaescu M (2023) Buckling critical pressures in collapsible tubes relevant for biomedical flows. Sci Rep 13(1):929. https://doi.org/10.1038/s41598-023-36513-6
5. Malkawi AH, Hinchliffe RJ, Xu Y, Holt PJ, Loftus IM, Thompson MM (2010) Patient-specific biomechanical profiling in abdominal aortic aneurysm development and rupture. J Vasc Surg 52(2):480–488. https://doi.org/10.1016/j.jvs.2010.01.029
6. Bäumler K, Vedula V, Sailer AM, Seo J, Chiu P, Mistelbauer G, Chan FP, Fischbein MP, Marsden AL, Fleischmann D (2020) Fluid-structure interaction simulations of patient-specific aortic dissection. Biomech Model Mechanobiol 19(5):1607–1628. https://doi.org/10.1007/s10237-020-01294-8
7. Jayendiran R, Nour B, Ruimi A (2018) Fluid-structure interaction (FSI) analysis of stent-graft for aortic endovascular aneurysm repair (EVAR): material and structural considerations. J Mech Behav Biomed Mater 87:95–110. https://doi.org/10.1016/j.jmbbm.2018.07.020
8. Raut SS, Jana A, De Oliveira V, Muluk SC, Finol EA (2013) The importance of patient-specific regionally varying wall thickness in abdominal aortic aneurysm biomechanics. J Biomech Eng 135(8):0810101–0810101. https://doi.org/10.1115/1.4024578
9. Scotti CM, Shkolnik AD, Muluk SC, Finol EA (2005) Fluid-structure interaction in abdominal aortic aneurysms: effects of asymmetry and wall thickness. Biomed Eng Online 4:6. https://doi.org/10.1186/1475-925X-4-64
10. Drewe CJ, Parker LP, Kelsey LJ, Norman PE, Powell JT, Doyle BJ (2017) Haemodynamics and stresses in abdominal aortic aneurysms: a fluid-structure interaction study into the effect of proximal neck and iliac bifurcation angle. J Biomech 60:150–156. https://doi.org/10.1016/j.jbiomech.2017.06.029
11. Hajirayat K, Gholampour SS, Sharifi I, Bizari D (2017) Biomechanical simulation to compare the blood hemodynamics and cerebral aneurysm rupture risk in patients with different aneurysm necks. J Appl Mech Tech Phys 58:968–974. https://doi.org/10.1134/S0021894417060025
12. Abbas S, Nasif M, Al-Waked R (2021) State-of-the-art numerical fluid-structure interaction methods for aortic and mitral heart valves simulations: a review. SIMULATION 98:003754972110235. https://doi.org/10.1177/00375497211023573
13. Bavo AM, Rocatello G, Iannaccone F, Degroote J, Vierendeels J, Segers P (2016) Fluid-structure interaction simulation of prosthetic aortic valves: comparison between immersed boundary and arbitrary Lagrangian-Eulerian techniques for the mesh representation. PLoS ONE 11(4):e0154517. https://doi.org/10.1371/journal.pone.0154517
14. Gao H, Feng L, Qi N, Berry C, Griffith BE, Luo X (2017) A coupled mitral valve-left ventricle model with fluid–structure interaction. Med Eng Phys 47:128–136. https://doi.org/10.1016/j.medengphy.2017.06.042
15. Lemmon JD, Yoganathan AP (2000) Three-dimensional computational model of left heart diastolic function with fluid-structure interaction. J Biomech Eng 122(2):109–111. https://doi.org/10.1115/1.429648
16. Mao W, Caballero A, McKay R, Primiano C, Sun W (2017) Fully-coupled fluid-structure interaction simulation of the aortic and mitral valves in a realistic 3D left ventricle model. PLoS ONE 12(9):e0184729. https://doi.org/10.1371/journal.pone.0184729
17. Idelsohn S, Oñate E, Pin FD (2004) The particle finite element method: a powerful tool to solve incompressible flows with free-surfaces and breaking waves. Int J Numer Meth Eng 61(7):964–989. https://doi.org/10.1002/nme.1096
18. Cremonesi M, Franci A, Idelsohn S, Oñate E (2020) A state of the art review of the particle finite element method (PFEM). Arch Comput Methods Eng 27(5):1709–1735. https://doi.org/10.1007/s11831-020-09468-4
19. Février S, Fernandez Sanchez EF, Lacroix M, Boman R, Ponthot JP (2024) Simulation of melt pool dynamics including vaporization using the particle finite element method. Comput Mech. https://doi.org/10.1007/s00466-024-02571-4
20. Rodríguez JM, Carbonell JM, Cante JC, Oliver J (2017) Continuous chip formation in metal cutting processes using the particle finite element method (PFEM). Int J Solids Struct 120:81–102. https://doi.org/10.1016/j.ijsolstr.2017.04.030
21. Rizzieri G, Ferrara L, Cremonesi M (2024) Numerical simulation of the extrusion and layer deposition processes in 3d concrete printing with the particle finite element method. Comput Mech 73(2):277–295. https://doi.org/10.1007/s00466-023-02367-y
22. Del Pin F, Huang CJ, Çaldichoury I, Paz RR (2020) On the performance and accuracy of PFEM-2 in the solution of biomedical benchmarks. Comput Particle Mech 7(1):121–138. https://doi.org/10.1007/s40571-019-00241-4
23. Geuzaine C, Remacle JF (2009) Gmsh: A 3-d finite element mesh generator with built-in pre- and post-processing facilities. Int J Numer Meth Eng 79(11):1309–1331. https://doi.org/10.1002/nme.2579
24. The CGAL Project (2023) CGAL user and reference manual, 5th edn. CGAL Editorial Board

25. Fernandez E, Février S, Lacroix M, Boman R, Papeleux L, Ponthot JP (2023) A particle finite element method based on level–set functions. J Comput Phys. https://doi.org/10.1016/j.jcp.2023.112187
26. Tezduyar TE, Mittal S, Ray SE, Shih R (1992) Incompressible flow computations with stabilized bilinear and linear equal-order-interpolation velocity-pressure elements. Comput Methods Appl Mech Eng 95(2):221–242. https://doi.org/10.1016/0045-7825(92)90141-6
27. Falla R, Bobach BJ, Boman R, Ponthot JP, Terrapon VE (2023) Mesh adaption for two-dimensional bounded and free-surface flows with the particle finite element method. Comput Particle Mech 10(5):1049–1076. https://doi.org/10.1007/s40571-022-00541-2
28. Ponthot JP, Metafor. http://metafor.ltas.ulg.ac.be/dokuwiki/. Accessed 24 Feb 2024
29. Ponthot JP (1995) Traitement unifié de la Mécanique des Milieux Continus Solides en Grandes Transformations par la Méthode des Eléments Finis. PhD thesis, publisher: Collection des publications de la faculté des Sciences Appliquées No 159, Université de Liège, https://orbi.uliege.be/handle/2268/5611
30. Fernández E, Février S, Lacroix M, Boman R, Ponthot JP (2023) Generalized-α scheme in the PFEM for velocity-pressure and displacement-pressure formulations of the incompressible Navier-Stokes equations. Int J Numer Methods Eng 124(1):40–78. https://doi.org/10.1002/nme.7101
31. Chung J, Hulbert GM (1993) A time integration algorithm for structural dynamics with improved numerical dissipation: the generalized-α method. J Appl Mech 60(2):37. https://doi.org/10.1115/1.2900803
32. Cerquaglia ML, Thomas D, Boman R, Terrapon V, Ponthot JP (2019) A fully partitioned Lagrangian framework for FSI problems characterized by free surfaces, large solid deformations and displacements, and strong added-mass effects. Comput Methods Appl Mech Eng 348:409–442. https://doi.org/10.1016/j.cma.2019.01.021
33. Lacroix M, Février S, Fernández E, Papeleux L, Boman R, Ponthot JP (2024) A comparative study of interpolation algorithms on non-matching meshes for PFEM-FEM fluid-structure interactions. Comput Math Appl 155:51–65. https://doi.org/10.1016/j.camwa.2023.11.045
34. Küttler U, Wall WA (2008) Fixed-point fluid–structure interaction solvers with dynamic relaxation. Comput Mech 43(1):61–72. https://doi.org/10.1007/s00466-008-0255-5
35. Bogaers A, Kok S, Reddy B, Franz T (2014) Quasi-newton methods for implicit black-box FSI coupling. Comput Methods Appl Mech Eng 279:113–132. https://doi.org/10.1016/j.cma.2014.06.033
36. Scheufele K, Mehl M (2017) Robust multisecant quasi-newton variants for parallel fluid-structure simulations–and other multiphysics applications. SIAM J Sci Comput 39(5):S404–S433. https://doi.org/10.1137/16M1082020
37. Thomas D, Cerquaglia ML, Boman R, Economon TD, Alonso JJ, Dimitriadis G, Terrapon VE (2019) SoftwCUPyDO—an integrated Python environment for coupled fluid-structure simulations. Adv Eng 128:69–85. https://doi.org/10.1016/j.advengsoft.2018.05.007
38. Pop G, Duncker DJ, Gardien M, Vranckx P, Versluis S, Hasan D, Slager CJ (2002) The clinical significance of whole blood viscosity in (cardio)vascular medicine. Neth Heart J 10(12):512–516
39. Schmid-Schönbein H, Wells RE (1971) Rheological properties of human erythrocytes and their influence upon the "anomalous" viscosity of blood. Ergeb Physiol Biol Chem Exp Pharmakol 63:146–216. https://doi.org/10.1007/BFb0047743
40. Grotberg JB (2021) Biofluid Mechanics | Biomedical engineering. Cambridge Text in Biomedical Engineering, Cambridge University Press
41. Bessonov N, Sequeira A, Simakov S, Vassilevskii Y, Volpert V (2016) Methods of blood flow modelling. Math Model Nat Phenomena 11(1):1–2. https://doi.org/10.1051/mmnp/201611101
42. Shahzad H, Wang X, Ghaffari A, Iqbal K, Hafeez MB, Krawczuk M, Wojnicz W (2022) Fluid structure interaction study of non-Newtonian Casson fluid in a bifurcated channel having stenosis with elastic walls. Sci Rep 12(1):1221. https://doi.org/10.1038/s41598-022-16213-3
43. Saeedi M, Shamloo A, Mohammadi A (2019) Fluid-structure interaction simulation of blood flow and cerebral aneurysm: effect of partly blocked vessel. J Vasc Res 56(6):296–307. https://doi.org/10.1159/000503786
44. Khanafer KM, Bull JL, Berguer R (2009) Fluid–structure interaction of turbulent pulsatile flow within a flexible wall axisymmetric aortic aneurysm model. Eur J Mech B Fluids 28(1):88–102. https://doi.org/10.1016/j.euromechflu.2007.12.003
45. Simsek FG, Kwon YW (2015) Investigation of material modeling in fluid–structure interaction analysis of an idealized three-layered abdominal aorta: aneurysm initiation and fully developed aneurysms. J Biol Phys 41(2):173–201. https://doi.org/10.1007/s10867-014-9372-x
46. Ariane M, Allouche MH, Bussone M, Giacosa F, Bernard F, Barigou M, Alexiadis A (2017) Discrete multi-physics: a mesh-free model of blood flow in flexible biological valve including solid aggregate formation. PLoS ONE 12(4):e017479. https://doi.org/10.1371/journal.pone.0174795
47. De Hart J, Peters GW, Schreurs PJ, Baaijens FP (2000) A two-dimensional fluid-structure interaction model of the aortic valve [correction of value]. J Biomech 33(9):1079–1088. https://doi.org/10.1016/s0021-9290(00)00068-3
48. Gharaie SH, Mosadegh B, Morsi Y (2018) In vitro validation of a numerical simulation of leaflet kinematics in a polymeric aortic valve under physiological conditions. Cardiovasc Eng Technol 9(1):42–52. https://doi.org/10.1007/s13239-018-0340-7
49. Ponthot JP (2002) Unified stress update algorithms for the numerical simulation of large deformation elasto-plastic and elasto-viscoplastic processes. Int J Plast 18(1):91–126. https://doi.org/10.1016/S0749-6419(00)00097-8
50. Manchester EL, Pirola S, Salmasi MY, O'Regan DP, Athanasiou T, Xu XY (2021) Analysis of turbulence effects in a patient-specific aorta with aortic valve stenosis. Cardiovasc Eng Technol 12(4):438–453. https://doi.org/10.1007/s13239-021-00536-9
51. Nobari S, Mongrain R, Leask R, Cartier R (2013) The effect of aortic wall and aortic leaflet stiffening on coronary hemodynamic: a fluid-structure interaction study. Med Biol Eng Comput 51(8):923–936. https://doi.org/10.1007/s11517-013-1066-1
52. Meduri S (2019) A fully explicit Lagrangian finite element method for highly nonlinear fluid-structure interaction problems. PhD thesis. Politecnico di Milano. https://www.politesi.polimi.it/handle/10589/145705?mode=full
53. Ghasemi Pour MJ, Hassani K, Khayat M, Etemadi Haghighi S (2022) Modeling of aortic valve stenosis using fluid-structure interaction method. Perfusion 37(4):367–376. https://doi.org/10.1177/0267659121998549
54. Yoganathan AP, He Z, Casey Jones S (2004) Fluid mechanics of heart valves. Annu Rev Biomed Eng 6:331–362. https://doi.org/10.1146/annurev.bioeng.6.040803.140111
55. Hatoum H, Dasi LP (2019) Spatiotemporal complexity of the aortic sinus vortex as a function of leaflet calcification. Ann Biomed Eng 47(4):1116–1128. https://doi.org/10.1007/s10439-019-02224-1
56. Saikrishnan N, Yap CH, Milligan NC, Vasilyev NV, Yoganathan AP (2012) In vitro characterization of bicuspid aortic valve hemodynamics using particle image velocimetry. Ann Biomed Eng 40(8):1760–1775. https://doi.org/10.1007/s10439-012-0527-2

57. Moore BL, Dasi LP (2015) Coronary flow impacts aortic leaflet mechanics and aortic sinus hemodynamics. Ann Biomed Eng 43(9):2231–2241. https://doi.org/10.1007/s10439-015-1260-4
58. Kivi AR, Sedaghatizadeh N, Cazzolato BS, Zander AC, Nelson AJ, Roberts-Thomson R, Yoganathan A, Arjomandi M (2020) Hemodynamics of a stenosed aortic valve: effects of the geometry of the sinuses and the positions of the coronary ostia. Int J Mech Sci 188:106015. https://doi.org/10.1016/j.ijmecsci.2020.106015
59. Amindari A, Saltik L, Kirkkopru K, Yacoub M, Yalcin HC (2017) Assessment of calcified aortic valve leaflet deformations and blood flow dynamics using fluid-structure interaction modeling. Inform Med Unlocked 9:191–199. https://doi.org/10.1016/j.imu.2017.09.001
60. Kim W, Choi H (2019) Immersed boundary methods for fluid-structure interaction: a review. Int J Heat Fluid Flow 75:301–309. https://doi.org/10.1016/j.ijheatfluidflow.2019.01.010
61. Mills CJ, Gabe IT, Gault JH, Mason DT, Ross J, Braunwald E, Shillingford JP (1970) Pressure-flow relationships and vascular impedance in man. Cardiovasc Res 4(4):405–417. https://doi.org/10.1093/cvr/4.4.405
62. Finol EA, Amon CH (2002) Flow-induced wall shear stress in abdominal aortic aneurysms: part I-steady flow hemodynamics. Comput Methods Biomech Biomed Engin 5(4):309–318. https://doi.org/10.1080/1025584021000009742
63. Stenmark KR, Yeager ME, El Kasmi KC, Nozik-Grayck E, Gerasimovskaya EV, Li M, Riddle SR, Frid MG (2013) The adventitia: essential regulator of vascular wall structure and function. Annu Rev Physiol 75:23–47. https://doi.org/10.1146/annurev-physiol-030212-183802
64. Xie J, Zhou J, Fung YC (1995) Bending of blood vessel wall: stress-strain laws of the intima-media and adventitial layers. J Biomech Eng 117(1):136–145. https://doi.org/10.1115/1.2792261
65. Thieret M (2008) Biology and mechanics of blood flows—part I: biology. Springe. https://doi.org/10.1007/978-0-387-74847-4
66. Sakalihasan N, Limet R, Defawe OD (2005) Abdominal aortic aneurysm. Lancet 365(9470):1577–1589. https://doi.org/10.1016/S0140-6736(05)66459-8
67. Malek AM, Alper SL, Izumo S (1999) Hemodynamic shear stress and its role in atherosclerosis. JAMA 282(21):2035–2042. https://doi.org/10.1001/jama.282.21.2035
68. Venkatasubramaniam AK, Fagan MJ, Mehta T, Mylankal KJ, Ray B, Kuhan G, Chetter IC, McCollum PT (2004) A comparative study of aortic wall stress using finite element analysis for ruptured and non-ruptured abdominal aortic aneurysms. Eur J Vasc Endovasc Surg 28(2):168–176. https://doi.org/10.1016/j.ejvs.2004.03.029
69. Greenhalgh RM, Brown LC, Powell JT, Thompson SG, Epstein D, Sculpher MJ, United Kingdom EVAR Trial Investigators (2010) Endovascular versus open repair of abdominal aortic aneurysm. N Engl J Med 362(20):1863–1871. https://doi.org/10.1056/NEJMoa0909305
70. Moll FL, Powell JT, Fraedrich G, Verzini F, Haulon S, Waltham M, van Herwaarden JA, Holt P, van Keulen JW, Rantner B et al (2011) Management of abdominal aortic aneurysms clinical practice guidelsoines of the European society for vascular surgery. Eur J Vasc Endovasc Surg 41(Suppl 1):S1–S58. https://doi.org/10.1016/j.ejvs.2010.09.011
71. Friesen J, Bergner J, Khan M, Triess S, Zoll A, Pelz PF, Adili F (2021) Comparison of existing aneurysm models and their path forward. Comput Methods Programs Biomed Update 1:100019. https://doi.org/10.1016/j.cmpbup.2021.100019
72. Darling RC, Messina CR, Brewster DC, Ottinger LW (1977) Autopsy study of unoperated abdominal aortic aneurysms. The case for early resection. Circulation 56(3 Suppl):II161–II164
73. Fillinger MF, Marra SP, Raghavan ML, Kennedy FE (2003) Prediction of rupture risk in abdominal aortic aneurysm during observation: wall stress versus diameter. J Vasc Surg 37(4):724–732. https://doi.org/10.1067/mva.2003.213
74. Haller SJ, Azarbal AF, Rugonyi S (2020) Predictors of abdominal aortic aneurysm risks. Bioengineering 7(3):79. https://doi.org/10.3390/bioengineering7030079
75. Fillinger MF, Raghavan ML, Marra SP, Cronenwett JL, Kennedy FE (2002) In vivo analysis of mechanical wall stress and abdominal aortic aneurysm rupture risk. J Vasc Surg 36(3):589–597. https://doi.org/10.1067/mva.2002.125478
76. Wang X, Ghayesh MH, Kotousov A, Zander AC, Amabili M, Dawson JA, Psaltis PJ (2023) Biomechanics of abdominal aortic aneurysm in the framework of Windkessel effect and fully-developed inflow velocity via two-way non-linear FSI. Int J Non-Linear Mech 157:104517. https://doi.org/10.1016/j.ijnonlinmec.2023.104517
77. Raghavan ML, Vorp DA (2000) Toward a biomechanical tool to evaluate rupture potential of abdominal aortic aneurysm: identification of a finite strain constitutive model and evaluation of its applicability. J Biomech 33(4):475–482. https://doi.org/10.1016/s0021-9290(99)00201-8
78. Singh TP, Moxon JV, Gasser TC, Golledge J (2021) Systematic review and meta-analysis of peak wall stress and peak wall rupture index in ruptured and asymptomatic intact abdominal aortic aneurysms. J Am Heart Assoc Cardiovasc Cerebrovasc Dis 10(8):e01977. https://doi.org/10.1161/JAHA.120.019772
79. Vande Geest JP, Wang D, Wisniewski SR, Makaroun MS, Vorp DA (2006) Towards a noninvasive method for determination of patient-specific wall strength distribution in abdominal aortic aneurysms. Ann Biomed Eng 34(7):1098–110. https://doi.org/10.1007/s10439-006-9132-6
80. Vorp DA (2007) Biomechanics of abdominal aortic aneurysm. J Biomech 40(9):1887–1902. https://doi.org/10.1016/j.jbiomech.2006.09.003
81. Ponthot JP, Boman R, Jeunechamps PP, Papeleux L, Deliege G (2013) An implicit erosion algorithm for the numerical simulation of metallic and composite materials submitted to high strain rates. In: Proceedings of the Indian National Science Academy 79:519. https://doi.org/10.16943/ptinsa/2013/v79i4/47987
82. Crompton MR (1966) Mechanism of growth and rupture in cerebral berry aneurysms. BMJ 1(5496):1138–1142
83. Scotti CM, Jimenez J, Muluk SC, Finol EA (2008) Wall stress and flow dynamics in abdominal aortic aneurysms: finite element analysis versus fluid-structure interaction. Comput Methods Biomech Biomed Engin 11(3):301–32. https://doi.org/10.1080/10255840701827412
84. Doyle BJ, Corbett TJ, Callanan A, Walsh MT, Vorp DA, McGloughlin TM (2009) An experimental and numerical comparison of the rupture locations of an abdominal aortic aneurysm. J Endovasc Ther 16(3):322–33. https://doi.org/10.1583/09-2697.1
85. Smagorinsky J (1963) General circulation experiments with the primitive equations: I the basic experiment. Mon Weather Rev 91(3):99–164. https://doi.org/10.1175/1520-0493(1963)091<0099:GCEWTP>2.3.CO;2